UNIVERSIDAD DE INVESTIGACIÓN DE TECNOLOGÍA EXPERIMENTAL YACHAY

Escuela de Ciencias Físicas y Nanotecnología

TÍTULO: Unravelling the multi-scale and turbulent structure of galactic winds

Trabajo de integración curricular presentado como
requisito para la obtención
del título de Físico

Autor:

Andrés Santiago Villares Guanga

Tutor:

Ph.D Wladimir Banda

Co - Tutor:

Ph.D Clara Rojas

Urcuquí, Julio 2023

AUTORÍA

Yo, **Villares Guanga Andrés Santiago**, con cédula de identidad **0105069298**, declaro que las ideas, juicios, valoraciones, interpretaciones, consultas bibliográficas, definiciones y conceptualizaciones expuestas en el presente trabajo; así cómo, los procedimientos y herramientas utilizadas en la investigación, son de absoluta responsabilidad de el/la autora (a) del trabajo de integración curricular. Así mismo, me acojo a los reglamentos internos de la Universidad de Investigación de Tecnología Experimental Yachay.

Urcuquí, Julio 2023.

Firmado electrónicamente por:
ANDRES SANTIAGO
VILLARES GUANGA

Andrés Santiago Villares Guanga
CI: 0105069298

AUTORIZACIÓN DE PUBLICACIÓN

Yo, **Villares Guanga Andrés Santiago,** con cédula de identidad **0105069298**, cedo a la Universidad de Investigación de Tecnología Experimental Yachay, los derechos de publicación de la presente obra, sin que deba haber un reconocimiento económico por este concepto. Declaro además que el texto del presente trabajo de titulación no podrá ser cedido a ninguna empresa editorial para su publicación u otros fines, sin contar previamente con la autorización escrita de la Universidad.

Asimismo, autorizo a la Universidad que realice la digitalización y publicación de este trabajo de integración curricular en el repositorio virtual, de conformidad a lo dispuesto en el Art. 144 de la Ley Orgánica de Educación Superior

Urcuquí, Julio 2023.

Firmado electrónicamente por:
ANDRES SANTIAGO
VILLARES GUANGA

Andrés Santiago Villares Guanga
CI: 0105069298

Dedication

To my brother and sister.

Acknowledgements

To all those who have supported me throughout my college journey. Especially, to my family, for their patience and love, to my advisor, Wladimir, for his invaluable guidance and friendship, and to my co-advisor Clara, for her kindness and assistance.

The author of this thesis and collaborators gratefully acknowledge the Gauss Centre for Supercomputing e.V. (`www.gauss-centre.eu`) for funding this project by providing computing time (via grant pn34qu) on the GCS Supercomputer SuperMUC-NG at the Leibniz Supercomputing Centre (`www.lrz.de`). In addition, the author acknowledges CEDIA (`www.cedia.edu.ec`) for providing access to their HPC cluster and for the technical support and expertise provided by CEDIA's staff.

Resumen

Los vientos galácticos son flujos multifásicos de energía y materia que salen de las galaxias con formación estelar. Las observaciones de las líneas de emisión y absorción revelan que estos vientos son multifásicos y turbulentos. Contienen componentes moleculares, atómicos e ionizados caracterizados por diferentes densidades y temperaturas. La fase caliente de los vientos galácticos suele encontrarse con cúmulos interestelares de gas frío y nubes de polvo. Sin embargo, la detección de gas frío a distancias significativas de los centros de las galaxias es un misterio, dada la facilidad con la que las nubes frías pueden perturbarse. Por tanto, las simulaciones numéricas son esenciales para comprender los procesos físicos subyacentes a la supervivencia del gas frío. En este proyecto, llevamos a cabo un conjunto de simulaciones hidrodinámicas en 3D de un viento supersónico que interactúa con una disposición de múltiples nubes que viajan juntas. Estudiamos cómo influyen en su evolución el enfriamiento radiativo y las diferentes distancias de separación entre nubes. Descubrimos que el tiempo de vida del material denso y frío en las nubes radiativas es mayor que en sus homólogas adiabáticas. Esto se atribuye a la condensación del gas caliente, que sostiene eficazmente el gas denso en el flujo. Cuando las nubes están más separadas, es más probable que generen inestabilidades dinámicas, lo que conduce a mayores grados de mezcla y destrucción del gas denso. Por el contrario, cuando las nubes están más cerca, el mecanismo de condensación es especialmente importante debido al apantallamiento hidrodinámico, que ayuda a mantener el material frío durante toda la evolución. La velocidad de las nubes disminuye a medida que disminuye la distancia de separación entre nubes, ya que esta disposición provoca la generación de grandes densidades de columna. De este modo, el apantallamiento hidrodinámico y el enfriamiento radiativo resultan eficaces para mantener el gas denso frío durante largos periodos de tiempo.

Palabras claves: Blindaje hidrodinámico, turbulencia, condensación, filamentos.

Abstract

Galactic winds are multi-phase outflows of energy and matter leaving star-forming galaxies. Emission and absorption line observations reveal that these winds are multiphase and turbulent. They contain molecular, atomic, and ionised components characterized by different densities and temperatures. The hot phase of galactic winds typically encounters interstellar clumps of cold gas and dust clouds. However, the detection of cold gas at significant distances from the centres of galaxies is a mystery given the ease with which cold clouds can be disrupted. Therefore, numerical simulations are essential to comprehend the underlying physical processes behind cold gas survival. In this project, we carry out a suite of 3D hydrodynamical simulations of a supersonic wind interacting with a multi-cloud arrangement of multiple clouds travelling together. We study how radiative cooling and different cloud separation distances influence their evolution. We find that the lifetime of dense and cold material in radiative clouds is longer than in their adiabatic counterparts. This is attributed to the condensation of warm gas, which effectively sustains the dense gas in the flow. When clouds are further apart, they are more likely to generate dynamical instabilities, leading to higher degrees of mixing and dense gas destruction. Conversely, when clouds are closer, the condensation mechanism is particularly important owing to hydrodynamic shielding, which helps to maintain the cold material throughout the entire evolution. The velocity of the clouds decreases as the cloud separation distance decreases, as this arrangement triggers the generation of large column densities. Hydrodynamic shielding and radiative cooling are thus found to be effective in maintaining cold dense gas for extended periods of time.

Keywords: Hydrodynamic shielding, turbulence, condensation, filaments.

Contents

List of Figures **x**

List of Tables **xii**

1 Introduction **1**
- 1.1 Problem Statement 4
- 1.2 General and Specific Objectives 4

2 Theoretical Background **5**
- 2.1 Stellar-driven Galactic Winds 5
- 2.2 Wind-Multicloud Systems 9
  - 2.2.1 Definitions 9
- 2.3 Hydrodynamic Shielding 11
- 2.4 Radiative Cooling 11

3 Methodology **13**
- 3.1 Software 13
  - 3.1.1 The PLUTO Code 13
  - 3.1.2 Python 13
  - 3.1.3 Computational requirements 14
- 3.2 Simulation Set-up 14
  - 3.2.1 Wind-multicloud Simulations 14
  - 3.2.2 Initial and Boundary Conditions 15
- 3.3 Diagnostics 17

4 Results & Discussion **21**
- 4.1 Global evolution 21
  - 4.1.1 Evolution of a wind-multicloud system 21
  - 4.1.2 The Role of Radiative Cooling 25

4.1.3 Thermodynamic Evolution of the Cloud Gas 25
4.1.4 Cloud Dynamics and Survival 27
4.2 Hydrodynamic Shielding 29
4.2.1 The Role of Hydrodynamic Shielding 29
4.2.2 On the effects of the separation distance, δ, between clouds 29
4.2.3 Cloud Dynamics and Survival 35
4.2.4 Implications for the Physics of Galactic Winds 37
4.3 Convergence Analysis and Limitations 39
4.3.1 Numerical Convergence 39
4.3.2 Limitations of our Study 42

5 Conclusions & Outlook **45**

Bibliography **49**

List of Figures

1.1 Diagram of the CGM taken from Tumlinson et al. 2017[1]. The CGM acts as a bridge between the ISM (space between stars within a galaxy) and the IGM (vast regions of space between galaxies). Galactic winds (orange) gradually emerge from the galactic disk while accreting gas (blue) feeds the galaxy with material from the IGM. 2

2.1 The steady-state wind solution for the CC85 model as a function of radius $r_* = r/R$ where R is the radius of the wind launching region. The intersection between the dimensionless parameters and the red vertical dashed lines ($\mathrm{Log}_{10}(r_*) = 0.3$) represent the initial conditions chosen for the simulations (see Section 3.2) 7

2.2 Three-dimensional simulations of the normalized cloud gas density of a wind-cloud model (left) taken from Banda-Barragan et al. 2019[2] and the number density of a wind-multicloud model (right) from the present thesis project (see Chapter 4). 10

3.1 Three-dimensional setup of our wind-multicloud models featuring the initial positions of a collection of spherical clouds, each separated from one another by a uniform distance of $\delta = 4$, $\delta = 16$, and $\delta = 32$ respectively. In addition, arrows illustrate the uniform velocity field that represents the galactic wind. 16

3.2 Net cooling rate ($|\Lambda/n_{\mathrm{H}}^2|$), normalized and expressed in absolute terms as a function of gas temperature 17

4.1 Two-dimensional slices at Z = 0 of the temperature in the adiabatic (top) and radiative (bottom) models at five different times through the simulation (columns). 22

4.2 Two-dimensional slices at Z = 0 of the thermal pressure in units of P/k_b in the adiabatic (top) and radiative (bottom) models at five different times through the simulation (columns). 23

4.3 Two-dimensional slices at Z = 0 of the number density in the adiabatic (top) and radiative (bottom) models at five different times through the simulation (columns). 24

4.4 Mass-weighted phase diagrams displaying the two-dimensional distributions of temperature and density of cloud material in the adiabatic (top) and radiative (bottom) $\delta = 16$ model. 26

4.5 Time evolution of the mass-weighted average temperature (left panel), mean density (middle panel), and dense gas mass fraction (right panel) of cloud material in both the adiabatic and radiative $\delta = 16$ model. 27
4.6 Time evolution of the mixing fraction, cold gas mass fraction, and mass-weighted average velocity of cloud material in the adiabatic and radiative $\delta = 16$ models. 28
4.7 Two-dimensional slices of the number density in adiabatic models with different separation values $\delta = 2$ (top panel), $\delta = 4$ (medium panel), and $\delta = 8$ (bottom panel) at five different times through the simulation (columns). 30
4.8 Two-dimensional slices of the number density in adiabatic models with different separation values $\delta = 16$ (top panel), $\delta = 32$ (medium panel), and $\delta = 64$ (bottom panel) at five different times through the simulation (columns). 31
4.9 Two-dimensional slices of the number density in radiative models with different separation values $\delta = 2$ (top panel), $\delta = 4$ (medium panel), and $\delta = 8$ (bottom panel) at five different times through the simulation (columns). 32
4.10 Two-dimensional slices of the number density in radiative models with different separation values $\delta = 16$ (top panel), $\delta = 32$ (medium panel), and $\delta = 64$ (bottom panel) at five different times through the simulation (columns). 33
4.11 Time evolution of the mass-weighted average temperature (top panels), mean density (medium panels), and dense gas mass fraction (bottom panels) for different values of the parameter δ in the adiabatic (left column) and radiative (right column) models. 34
4.12 Time evolution of the mixing fraction (top panels), cold gas mass fraction (medium panels), and mass-weighted average velocity (bottom panels) for different values of the parameter δ in the adiabatic (left column) and radiative (right column) models. 36
4.13 Convergence Analysis of the time evolution of the mass-weighted average temperature, mean density, dense gas mass fraction, mixing fraction, cold gas mass fraction, and mass-weighted average velocity of the adiabatic model for $\delta = 8$ (top two rows) and $\delta = 16$ (last two rows). 40
4.14 Convergence Analysis of the time evolution of the mass-weighted average temperature, mean density, dense gas mass fraction, mixing fraction, cold gas mass fraction, and mass-weighted average velocity of the radiative model for $\delta = 8$ (top two rows) and $\delta = 16$ (last two rows). 41

List of Tables

3.1 Overview of the simulation parameters chosen for different models. Columns 1 and 2 respectively indicate the type of thermodynamic model introduced for the simulation and the resolution in units of X (number of cells per cloud radius with the standard notation, R_x). Columns 3 and 4 indicate the number of cells in the 3D domain and the density contrast between the clouds and the wind. Columns 5 and 6 indicate the cooling floor and the distance between clouds given by the dimensionless parameter δ (see Section 2.3 for the definition). 18

Chapter 1

Introduction

Galaxies are dynamic, complex systems that continuously change over time. They interact with other galaxies in their galactic group, preventing them from being isolated systems. The rate of star formation and the amount of dust and gas ejected via winds are key factors in the evolution of galaxies. Molecular gas in the interstellar medium (ISM, i.e. in the disc of star-forming galaxies) serves as the fuel for star formation (SF) which constitutes a type of feedback process, which results in large-scale galactic winds. Such winds populate the circumgalactic medium (CGM) and remove metals from the disc of galaxies, depositing them outside of the host galaxies (see Shopbell & Bland-Hawthorn 1998[3]). These feedback processes are produced by star formation events such as supernova explosions, which launch galactic winds, as well as by stellar wind bubbles and active galactic nuclei (AGN) events involving AGN winds, radiative pressure, and astrophysical jets (see e.g. Scannapieco et al. 2001[4]; Kaviraj et al. 2017[5]).

As a result of SF feedback, heavy elements produced by nuclear processes in stars and supernovae within galaxies are deposited in both the CGM and the intergalactic medium (IGM). The transition region between the area where star formation occurs and the IGM is known as the galactic halo or the CGM. The evolution of the CGM is shaped by these feedback mechanisms, which have the ability to photoionize, collisionally heat, and chemically enrich the CGM. The CGM is a multi-phase environment that permits the exchange of energy and matter between the interstellar and the intergalactic media which in turn affects the overall gas content and metallicity of galaxies.

Galactic winds are complex, multifaceted outflows of matter and energy that come from star-forming galaxies (see Figure 1.1). These winds are made of molecular, atomic, and ionized components, each of which has unique density and temperature ranges. These winds are of great interest because they are one of the main ways by which galaxies can lose gas and metals, which has a big impact on how galaxies evolve. Many galaxies, especially starburst galaxies, have been examined at various wavelengths, revealing the presence of a considerably hot and diffuse gas component in which a cold, dense gas component is embedded, constituting the galactic winds (e.g., Shopbell & Bland-Hawthorn 1998[3]; Tripp et al. 2011[6]; Di Teodoro et al. 2018[7]; Salak et al. 2018[8]).

Galactic winds launched by feedback processes encounter a diverse range of clumps with varying sizes in the ISM. Interstellar clumps are typically constituted by gas, dust and sometimes by conglomerates of stars and solid

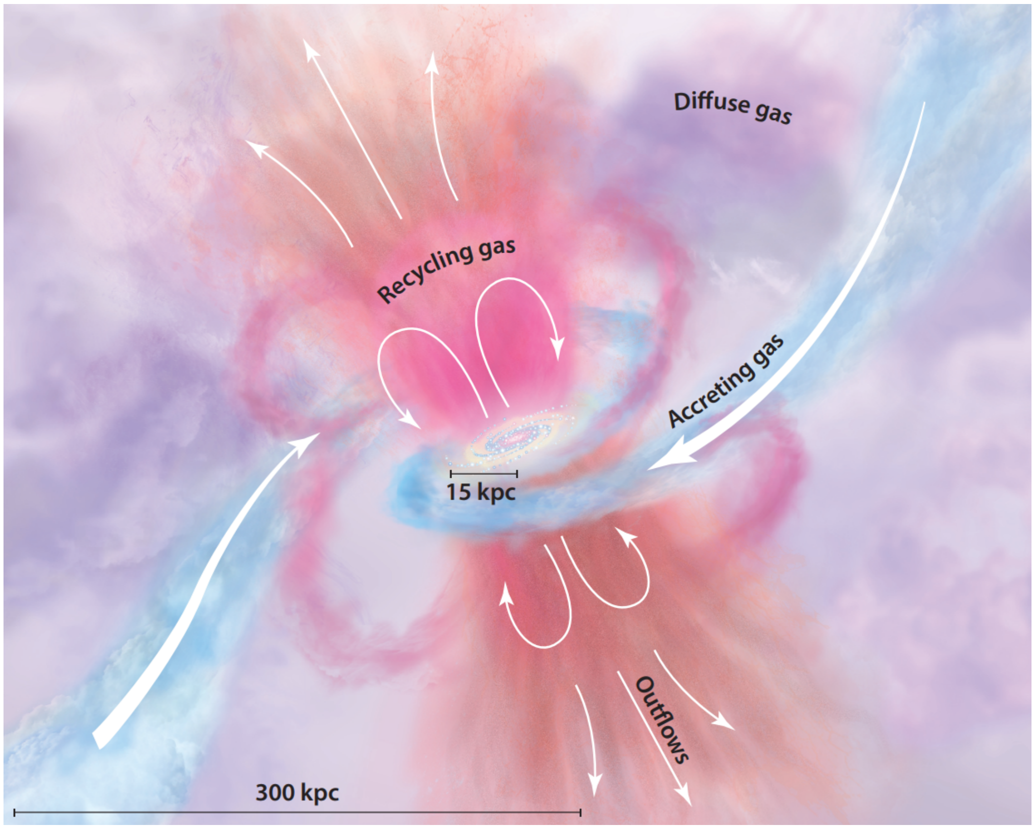

Figure 1.1: Diagram of the CGM taken from Tumlinson et al. 2017[1]. The CGM acts as a bridge between the ISM (space between stars within a galaxy) and the IGM (vast regions of space between galaxies). Galactic winds (orange) gradually emerge from the galactic disk while accreting gas (blue) feeds the galaxy with material from the IGM.

bodies. The interaction between winds and surrounding clouds results in significant alterations in the physical and chemical properties of both winds and clouds (e.g., Ballone et al. 2013[9]; Mendis & Horanayi 2014[10]). For example, when the outflowing material collides with atomic and dense clouds, the ram pressure exerted by the material compresses the clouds, leading to their disruption (see e.g. Klein, McKee & Colella 1994[11]). Moreover, the net force that results from the momentum transfer of the wind material to clouds can cause acceleration of the clouds (see Cottle et al. 2020[12]). This process acts upon the upstream side of the cloud, pushing dense material downstream and leading to its fragmentation (Gregori et al. 2000[13]).

Why is studying galactic winds important? A deeper comprehension of galactic winds can help us ascertain the radial distribution of metals from the galaxy's centre, the chemical enrichment of galaxies, and the sustainability of its star formation rate. Moreover, such understanding can help address the discrepancy between actual observations and the baryon fraction, namely the ratio of the mass of baryons to the total mass observed in the Universe (see Tumlinson et al. 2017[1]).

Considering the significance of galactic winds, for the ecology of the ISM and the CGM, and the global evolution of galaxies, it is crucial to gain a comprehensive understanding of the underlying physical processes that shape them. Therefore, numerical simulations of wind-cloud, wind-multicloud, and disc-wind interactions are essential tools to better understand the physical characteristics of the gas. As a result, a long history of numerical simulation studies of galactic wind-cloud interactions exists. These studies encompass a wide range of analyses that include hydrodynamic models and magnetohydrodynamic models with different resolutions and domain sizes (e.g. Banda-Barragan et al. 2020[14]; Schneider & Robertson 2017[15]). These models consist of establishing specific initial and boundary conditions, including the shape of the clouds, the distributions of multicloud systems, the density and magnetic properties of the gas, the speed of the wind, the arrangement of the clouds, and the inclusion or exclusion of radiative processes (i.e. radiative models)[16].

Adiabatic simulations have demonstrated that the hot wind has the ability to remove material from the clouds, eventually leading to their destruction via dynamical instabilities (see Nakamura et al. 2006[17]; Banda-Barragan et al. 2016[18]). These models show that clouds can be easily destroyed in galactic wind environments, thus posing some tension between simulations and astronomical observations, which show the existence of cold clouds at very large distances from the galactic planes. On the other hand, simulations that incorporate radiative cooling indicated that the lifetime of clouds can be significantly prolonged if this effect is efficient (see Cooper et al. 2009[16]; Sparre et al. 2019[19]), but they are idealised as they consider only isolated clouds. Moreover, simulations of groups of adiabatic clouds (i.e. multicloud systems) placed along a stream have demonstrated that hydrodynamical shielding can effectively extend their lifespan while simultaneously facilitating their acceleration (see Forbes & Lin 2019[20]; Banda-Barragan et al. 2020[14]). However, the radiative scenarios with supersonic winds have not been characterised before. Thus, in this thesis, we extend such previous studies to account for the effects of radiative cooling and supersonic winds in wind-multicloud systems.

Through these simulations, we can characterize the multiscale structure of galactic winds and analyze the thermodynamic and turbulent properties of the different gas phases associated with the changing outflow. To achieve this, we contrast different models that resemble actual astrophysical environments (particularly those of the CGM). Numerical simulations offer a powerful tool for researching the intricate physics of the CGM, including how the wind affects the morphology of clouds within multicloud systems and their subsequent evolution.

1.1 Problem Statement

Multiple intricate mechanisms take place during galaxy formation and evolution. Galactic winds constitute one of such mechanisms and play a key role in regulating the mass and metal content of galaxies. Wind-cloud models have played an important role in understanding the tight empirical relationship between clouds and the surrounding hot background. However, the ease with which cold clouds can be disrupted presents observational challenges. Surveys of quasar absorption lines have identified significant quantities of dense gas, i.e., gas with low ionization states in the neighbourhood of galaxies of various masses and types (see Tumlinson et al. 2011[21]; Pfuhl et al. 2015[22]; Casavecchia et al. 2023[23]). The detection of cold gas at significant distances from the centres of galaxies, ranging in the hundreds to tens of thousands of parsecs, is a mystery given the apparent ease with which cold clouds can be disrupted.

1.2 General and Specific Objectives

The aim of this thesis is to understand which mechanisms extend the lifetime of cold and dense clouds by conducting a series of three-dimensional adiabatic and radiative hydrodynamical simulations of winds interacting with multi-cloud complexes. The simulations will assess the ability of systems of clouds, travelling along a straight trajectory with an initial separation distance δ between them, to protect themselves against hydrodynamic drag and dynamical instabilities arising from their interactions with a hot supersonic wind gas. To reach this objective, the following specific goals need to be achieved:

- Characterise the evolution of wind-multicloud systems via hydrodynamical simulations of multicloud systems interacting with a hot supersonic wind gas.
- Explore the differences that arise when supersonic winds and radiative cooling are included in the simulations, compared to their subsonic and adiabatic counterparts (reported in earlier studies).
- Evaluate the efficiency of hydrodynamic shielding exhibited by models with different initial conditions.
- Contrast the thermodynamical evolution of multicloud systems with different cloud separation distances, δ.
- Discuss the effects of numerical resolution on the multicloud systems and the limitations of this work.

This thesis is structured as follows: Chapter 2 provides a brief explanation of the theoretical background of galactic winds and wind-multicloud systems, along with an introduction to the concepts of hydrodynamic shielding and radiative cooling. Chapter 3 outlines the methodology and initial conditions employed in the project, including the description of the software and computational tools used for simulations and data analysis. Chapter 4 presents the results obtained, provides a comprehensive discussion, compares them to previous studies, and discusses the effects of numerical resolution while also highlighting the limitations of the work. Finally, Chapter 5 summarizes the key findings of this thesis and provides final remarks.

Chapter 2

Theoretical Background

2.1 Stellar-driven Galactic Winds

To start, we will briefly discuss how galactic winds form and evolve, and what physical processes are important in them. Large-scale outflows of gas from a galaxy, referred to as stellar-driven galactic winds, are accelerated by the energetic emissions from stars within the host galaxy. Cosmic rays, supernova explosions triggered by the death of massive stars, and the radiation pressure of starlight scattering on dust particles are only a few of the mechanisms that might accelerate these winds (see Heckman & Thompson 2017[24]). The star formation rate (SFR) and the chemical enrichment of a galaxy are thought to be greatly influenced by galactic winds.

On the one hand, the ejection of gas from a galaxy by galactic winds might decrease the amount of material available for star formation, which may slow the SFR in the disc of the host galaxy. This effect can have a long-term impact on the galaxy's evolution, as it would affect the amount of mass converted into stars over time. On the other side, the introduction of heavy elements through these winds into the CGM and the IGM can enrich the gas and dust that eventually collapse to form new stars changing the metallicity of the new populations of stars and possibly increasing the SFR. These heavy elements are produced by stars via nuclear fusion, and they are essential for both star formation and the general chemical history of galaxies (see Krumholz et al. 2018[25]).

In a similar way, the amount of gas that is swept up, compressed and that can potentially lead to new star formation episodes, can depend on the properties of the wind. The nature of the wind, particularly its metallicity and particle content, might alter the chemical evolution of the surrounding gas and dust. Furthermore, winds may be quite important for the total chemical enrichment of a galaxy. Heavy elements like carbon, oxygen, and iron are produced by and released into the ISM when stars evolve and eventually die. The intergalactic medium can then be enriched by these elements (see e.g. Laganá et al. 2009[26]), which may also have an impact on the elemental composition of upcoming star generations. These elements can subsequently be swept away from the galaxy by new episodes of SF and galactic winds.

The formation of a galactic-scale "superbubble" occurs when the net energy produced by supernova explosions (SNe) is not efficiently dissipated by the multiphase ISM (see McKee & Ostriker 1977[27]). Then, multiple bubbles combine and form a coherent large-scale galactic wind. In contrast, if the energy can be effectively radiated and the outflowing gas does not reach the galactic escape velocity, a "galactic fountain" is produced. Such galactic fountains interact with the CGM gas (also called the galactic halo) and bring back material to the disc of the host galaxy. Despite the complexity of the physical processes involved in launching and propagating galactic winds through SNe, a simple and clear analytic model has been classically used to study these phenomena.

The classic model for SN-driven galactic winds was first developed by Chevalier and Clegg in 1985[28], and its commonly referred to as the CC85 model. This model considers the momentum injected by supernovae into the ISM, which drives the outflow of gas. It assumes a uniform density medium and a spherically symmetric distribution of supernovae. The model predicts that the velocity of the outflowing wind increases with distance from the galactic plane and that the mass loading factor, which measures the amount of mass carried away by the wind per unit mass of stars formed, decreases when higher SFR are considered.

When spherical symmetry is assumed and the effects of gravity, rotation, and radiative cooling are disregarded, the injection rates of total mass and energy into the wind are represented by $\dot{M}_{\rm hot}$ and $\dot{E}_{\rm hot}$, respectively. The equations that describe the steady-state hydrodynamics of a hot wind are given by:

$$\frac{1}{r^2}\frac{d}{dr}(\rho v r^2) = q, \tag{2.1}$$

$$v\frac{dv}{dr} = -\frac{1}{\rho}\frac{dP}{dr} - \frac{qv}{\rho}, \tag{2.2}$$

$$\frac{1}{r^2}\frac{d}{dr}\left[\rho v r^2\left(\frac{1}{2}v^2 + \frac{\gamma}{\gamma-1}\frac{P}{\rho}\right)\right] = Q, \tag{2.3}$$

where ρ is the density, r is the radial radius, v is the wind velocity, γ is the adiabatic index (see equation 2.17), and P is the pressure. For $r < R$, $q = \dot{M}_{hot}/V$, $Q = \dot{E}_{hot}/V$ where q and Q are the averaged injected efficiencies per unit volume, and $V = 4\pi R^3/3$ is the volume of the wind launching region with R being the radius of this region (see Chevalier & Clegg 1985[28]). For $r > R$, we have $q = Q = 0$, which implies that there is no injection of mass or energy by the wind beyond the radius R. The solutions obtained from equations (2.1) to (2.3) can be expressed using the Mach number of the wind M (see equation 2.18), as follows:

$$\left(\frac{3\gamma + 1/M^2}{1+3\gamma}\right)^{-(3\gamma+1)/(5\gamma+1)}\left(\frac{\gamma - 1 + 2/M^2}{1+\gamma}\right)^{(\gamma+1)/[2(5\gamma+1)]} = \frac{r}{R} \quad (r < R), \tag{2.4}$$

and

$$M^{2/(\gamma-1)}\left(\frac{\gamma - 1 + 2/M^2}{1+\gamma}\right)^{(\gamma+1)/[2(\gamma-1)]} = \left(\frac{r}{R}\right)^2 \quad (r \geq R), \tag{2.5}$$

The solution for the wind velocity as a function of the radius of the wind r can be represented in a dimensionless form by using the dimensionless radius, $r^* = r/R$. Additionally, the dimensionless velocity u_*, density ρ_*, pressure P_*, and temperature T_*, are also employed in this representation as follows:

$$u = u_* \dot{M}_{hot}^{-1/2}\dot{E}_{hot}^{1/2}, \tag{2.6}$$

$$\rho = \rho_* \dot{M}_{hot}^{3/2} \dot{E}_{hot}^{-1/2} R^{-2}, \tag{2.7}$$

$$P = P_* \dot{M}_{hot}^{1/2} \dot{E}_{hot}^{1/2} R^{-2}, \tag{2.8}$$

$$T = T_* \dot{M}_{hot} \dot{E}_{hot}^{-1} \mu^{-1} m_u^{-1} k_b, \tag{2.9}$$

where μ is the mean particle mass, m_u is the atomic mass unit, and k_b is the Boltzman constant.

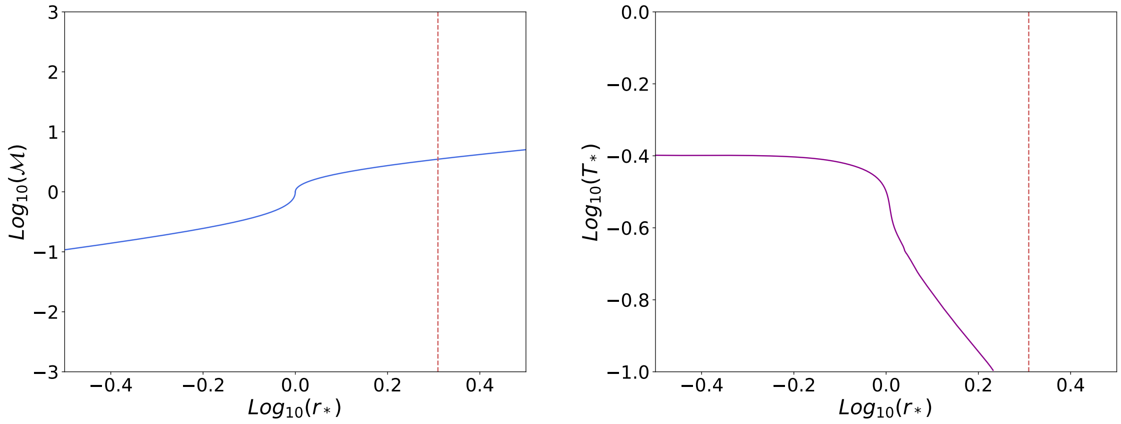
(a) Mach number

(c) Dimensionless temperature

(b) Dimensionless velocity

(d) Dimensionless density

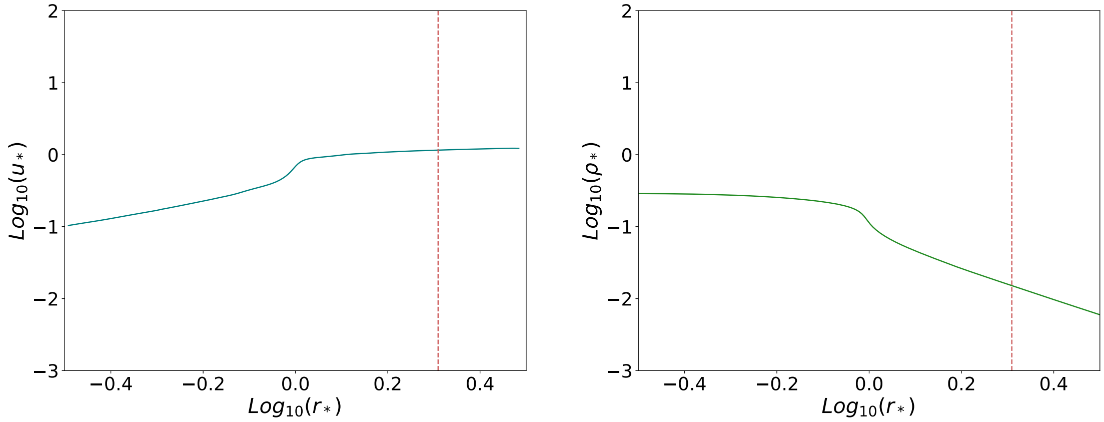

Figure 2.1: The steady-state wind solution for the CC85 model as a function of radius $r_* = r/R$ where R is the radius of the wind launching region. The intersection between the dimensionless parameters and the red vertical dashed lines ($\mathrm{Log}_{10}(r_*) = 0.3$) represent the initial conditions chosen for the simulations (see Section 3.2)

Figure 2.1 displays the analytical solutions for a selection of the dimensionless variables and Mach numbers. It is possible to introduce two dimensionless parameters, the thermalization efficiency α', which represents the fraction of energy released by an SNe that is converted into thermal energy, and the mass-loading rate β, which describes the efficiency of mass ejection from the galaxy. The values for those parameters are not fixed but rather depend on various factors such as the properties of the ISM, the distribution of SNe, and the specific mechanism driving the outflow (see Zhang 2014[29]). Therefore, it is expected that these parameters vary widely between different galaxies. These parameters are used to normalize the energy input and the mass-loading efficiency by

$$\dot{E}_{hot} = \alpha' \dot{E}_{SN}, \tag{2.10}$$

$$\dot{M}_{hot} = \beta \mathrm{SFR}, \tag{2.11}$$

where $\dot{E}_{SN}$ is the net energy rate provided by a SNe and it can be estimated by

$$\dot{E}_{SN} = e\nu \mathrm{SFR}, \tag{2.12}$$

where $e = 10^{51} e_{51}$ ergs represents the energy injected by a single SN and $\nu = (100 M_\odot)^{-1} \nu_{100}$ denotes the number of SNe per unit mass of star formation. Commonly, one SN explosion occurs for every $100 M_\odot$ of star formation, thus $\nu_{100} \simeq 1$ (see Strickland & Heckman 2009[30]). Therefore, we define

$$\alpha = \alpha' e_{51} \nu_{100}, \tag{2.13}$$

where the new thermalization efficiency is used to parametrize the energy injection rate. As a result, the temperature, number density, and velocity of the hot wind outflow are

$$T(r) = 6.3 \times 10^7 \mathrm{K} \mu \left(\frac{\alpha}{\beta}\right) \left[\frac{P_*(r_*)}{\rho_*(r_*)}\right], \tag{2.14}$$

$$n(r) = 1.4\,\mathrm{cm}^{-3} \alpha^{-1/2} \beta^{3/2} \mu^{-1} R_{200pc}^{-2} \rho_*(r_*) \mathrm{SFR}_0, \tag{2.15}$$

$$V(r) = 710\,\mathrm{km\,s}^{-1} \alpha^{1/2} \beta^{-1/2} u_*(r_*), \tag{2.16}$$

where $\mathrm{SFR}_0 = \mathrm{SFR}/(M_\odot \mathrm{yr}^{-1})$ and $R_{200pc} = R/(200pc)$.

One case of study is the starburst galaxy M82. Strickland & Heckman 2009[30] used the Chandra X-ray observatory to detect the presence of hot wind with temperatures of T$\sim 3 - 8 \times 10^7$ K. This allowed the thermalization efficiency and the mass-loading rate to be constrained as $\alpha \sim 0.3 - 1$ and $\beta \lesssim 2$, respectively (see Bustard et al. 2016[31]). For instance, Schneider & Robertson 2017[15] conducted a set of high-resolution hydrodynamical simulations that incorporated $\alpha = 0.33$ and $\beta = 1.42$ values within the acceptable range of fits. Therefore, the number density, velocity, pressure, and temperature of the CC85 wind model at $r = 1$ kpc used in those simulations were:

$$n_{wind} = 5.2626 \times 10^{-3} \mathrm{cm}^{-3}$$

$$v_{wind} = 1.1962 \times 10^{3} \mathrm{kms}^{-1}$$

$$P_{wind}/k = 1.9881 \times 10^{4} \mathrm{cm}^{-3} \mathrm{K}$$

$$T_{wind} = 3.7778 \times 10^{6} \mathrm{K}$$

2.2 Wind-Multicloud Systems

A wind-multicloud system is a generalisation of a wind-cloud system and constitutes an idealized scenario where an initially static, isolated cloud or a group of clouds interacts with a wind velocity field inside the boundaries of a finite volume (see Figure 2.2). The equations governing the dynamics of wind-cloud interactions also apply to wind-multicloud systems, and they are intrinsically nonlinear. This means that analytical solutions are typically only available in simplified cases. As such, numerical simulations are commonly employed to investigate these systems (see Alūzas et al. 2012[32]; Alūzas et al. 2014[33]). In particular, numerical simulations offer a means of studying the hydrodynamic instabilities that occur in the outer layers of clouds, which lead to their destruction. Moreover, these simulations can yield a detailed understanding of the manner in which various physical processes - such as radiative processes, magnetic fields, turbulence, and thermal conduction - impact the evolution of wind-swept clouds (e.g. Banda-Barragan et al. 2018[2]). Through numerical simulations, it is possible to explore how the interplay of these physical factors affects the shape, size, and behaviour of clouds under a range of different conditions.

2.2.1 Definitions

In the hydrodynamic context, wind-cloud and wind-multicloud systems are characterized by various quantities. One of the key quantities used to describe such systems is the adiabatic index of the gas within the cloud:

$$\gamma = \frac{c_p}{c_v}, \tag{2.17}$$

where c_p is the heat capacity at constant pressure and c_v is the heat capacity at constant volume. In the study of wind-cloud systems, this ratio is particularly important because it helps to describe the thermodynamical behaviour of the gas within the cloud as it interacts with the surrounding wind velocity field. This interaction can lead to complex gas flow patterns within the cloud and its surrounding environment. The Mach number of the wind is another important quantity that plays a crucial role in influencing the system's behaviour and is defined as:

$$\mathcal{M}_W = \frac{|v_W|}{c_W}, \tag{2.18}$$

where v_W is the speed of the wind and $c_W = \sqrt{\gamma \frac{P}{\rho_W}}$ is the adiabatic sound speed of the wind. When the Mach number is low (i.e., less than 0.3), the gas flow around the cloud is typically smooth and laminar. However, as the Mach number increases beyond this value, the flow becomes more turbulent and chaotic (e.g. Armillotta et al. 2017[34]), which can generate shocks and instabilities within the cloud (see Banda-Barragan et al. 2018[2]). An additional important parameter is the density contrast which is defined as:

$$\chi = \frac{\rho_c}{\rho_W}, \tag{2.19}$$

where ρ_c is the density of the cloud and ρ_W is the density of the surrounding medium. A higher density contrast indicates a more significant difference in density between the cloud and the surrounding medium, resulting in a more prolonged interaction between the two. This interaction can cause the cloud to experience more deformation,

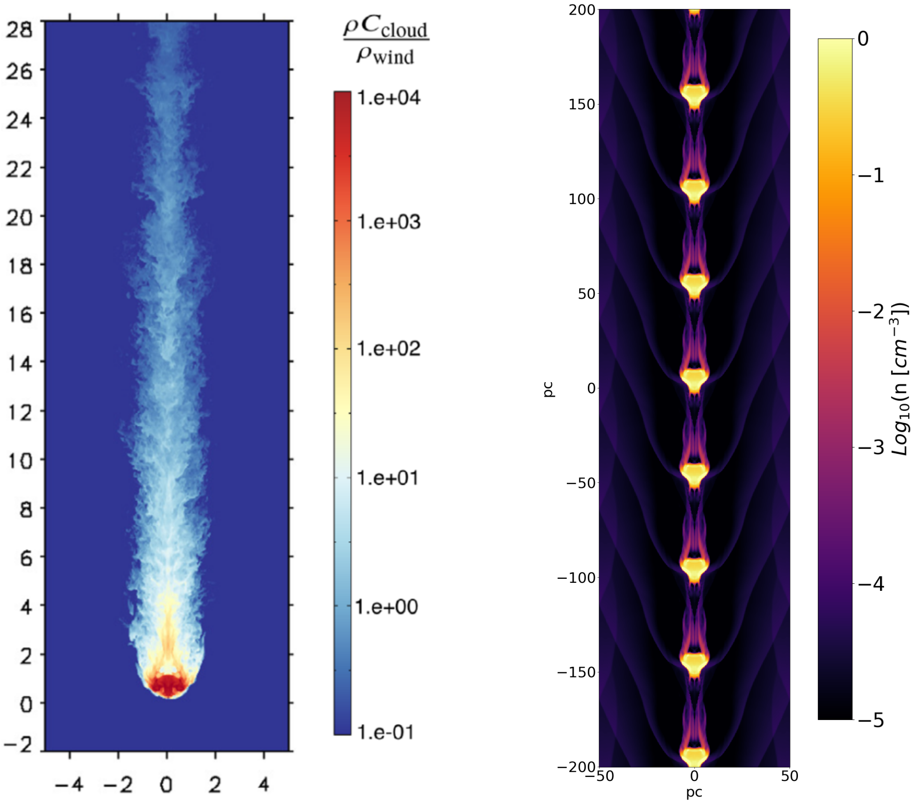
(a) Wind-cloud model

(b) Wind-multicloud model

Figure 2.2: Three-dimensional simulations of the normalized cloud gas density of a wind-cloud model (left) taken from Banda-Barragan et al. 2019[2] and the number density of a wind-multicloud model (right) from the present thesis project (see Chapter 4).

fragmentation, and dispersal (see Cooper et al 2009[16]). Finally, we introduce the concept of cloud crossing time, which represents the duration for a cloud to cross its own radius. This is defined as follows:

$$t_{\text{cross}} = \frac{r}{v_{\text{rel}}}, \tag{2.20}$$

where r represents the radius of the cloud, while v_{rel} represents the relative velocity of the cloud with respect to the wind.

2.3 Hydrodynamic Shielding

In the CGM, cold clouds with uniform density are commonly embedded in a less dense and hotter background gas. The simplest scenario describes the interaction between a single cold cloud and a hot wind gas. The cold cloud undergoes several processes as a consequence of its interaction with the less dense background. Initially, a shock compresses the cloud in the flow direction, exposing it to disruptions through hydrodynamic instabilities. Then, the cloud suffers drag which increases its velocity such that it approaches the velocity of the background flow[20].

Various observational surveys have revealed the presence of a substantial quantity of low-ionization gas in the proximity to galaxies (Tumlinson et al. 2011[21]). While some recent simulation studies reveal that absorption spectra can indeed be obtained in such environments (see de la Cruz et al. 2019[35]; Casavecchia et al. 2023[23]), the presence of such gas at considerable distances is an enigma considering the tendency of cold clouds to be destroyed by dynamical instabilities. Therefore, it is essential to introduce complementary physical mechanisms in order to provide a thorough and comprehensive explanation for the prolonged lifetime of cold clouds.

Hydrodynamic shielding is the process that exhibits the capability of a group of clouds moving in a straight trajectory to protect and shield themselves from hydrodynamic drag and potential disruptions caused by their interaction with the surrounding hot wind gas. The dimensionless parameter δ is introduced to describe the separation distance between cold clouds along the streaming direction. This parameter is determined by the ratio of the distance between the centres of the clouds to the radius of the clouds themselves:

$$\delta = \frac{\left|\vec{r}_i - \vec{r}_j\right|}{R}, \tag{2.21}$$

where $\vec{r}_i$ and $\vec{r}_j$ are the positions of the centres of two clouds, and R is the radius of each cloud. Adiabatic simulations by Forbes et al. 2019[20] that are independent of scale have indicated that clouds that move together in such streams can offer a certain degree of shielding against disruptions, provided that they are in close proximity to each other i.e. when the dimensionless parameter δ is small[20]. This suggests that the proximity of the clouds within the stream may play a crucial role in slowing down the rate at which the clouds' velocities approach the background velocity and develop instabilities. In our models, two types of instabilities can arise and influence cloud destruction:

- Kelvin-Helmholtz (KH) Instabilities: KH instabilities occur when two fluids are in relative motion, and the difference in tangential velocities on both sides of the gas interface creates perturbations in the form of vortices (see Kelvin 1871[36]; Helmholtz 1868[37]; Chandrasekhar 1961[38]).

- Rayleigh-Taylor (RT) Instabilities: RT instabilities arise when the interface between two fluids of different densities is subject to constant or time-dependent acceleration, where the low-density fluid accelerates into the denser fluid, thus forming finger-like structures (see Rayleigh 1882[39]; Taylor 1950[40]).

2.4 Radiative Cooling

Radiative cooling is a fundamental physical process that describes the release of energy in the form of electromagnetic radiation from a multi-phase gas, whose temperature decreases as energy is removed. The atmospheres of planets and stars, the ISM, the CGM, and the IGM are just a few astrophysical environments where this process is an essential component (see Draine 2011[41]).

The cooling rate of an object through radiative processes is influenced by various factors, including the density and temperature of the gas, the chemical composition (usually quantified as metallicity), the ionization balance, and the intensity and spectrum of the radiation field. In low-temperature gas ($T < 10^5$K), the cooling rate may be dominated by processes such as recombination, where free electrons combine with ions to form neutral atoms and the emission of spectral lines. In contrast, in high-temperature gas ($T > 10^7$K), the cooling rate may be dominated by processes such as bremsstrahlung (free-free emission), where free electrons are decelerated by the electric field of ions and emit electromagnetic radiation, and inverse Compton scattering, where high-energy photons interact with free electrons and lose energy. In the gas that has been heated to temperatures of $10^5\mathrm{K} \lesssim T < 10^7$K, also called warm-hot intergalactic medium (WHIM), the nature of the radiation field as well as the metallicity of the gas have a significant impact. The cooling of the WHIM is dominated by line radiation, the effects of photoionization and heavy elements (see Wiersma et al. 2009[42]).

The cooling rate is also influenced by the intensity and spectrum of the radiation field. For instance, in a region with a strong ultraviolet radiation field, the cooling rate may increase due to the enhanced photoionization and photoheating of the gas. In addition, the cooling rate may also depend on the type and energy of the radiation. For instance, X-rays and gamma rays can produce highly energetic electrons that, in turn, lead to more significant cooling rates than lower-energy photons, such as visible or ultraviolet light (see Smith et al. 2017[43]).

The cooling rate Λ_i measures the contribution of an element i that is heavier than helium to the substance's overall cooling rate. This rate is calculated by subtracting the cooling rate obtained using all elements from the cooling rate when the abundance of element i is set to zero, while all other abundances remain constant. The total net cooling rate can be obtained by:

$$\Lambda = \Lambda_{\mathrm{H,He}} + \sum_{i>\mathrm{He}} \Lambda_i, \tag{2.22}$$

where $\Lambda_{\mathrm{H,\,He}}$ is the combined cooling rate of hydrogen and helium, and the second term Λ_i represents the contribution of heavy elements i to the radiative cooling rate. Equation 2.22 can be rewritten as

$$\Lambda = \Lambda_{\mathrm{H,He}} + \sum_{i>\mathrm{He}} \frac{n_i/n_H}{(n_i/n_H)_\odot} \Lambda_{i,\odot}, \tag{2.23}$$

where $(n_i/n_H)_\odot$ is the solar abundance for element i and $\Lambda_{i,\odot}$ is the contribution of the heavy element i for solar abundance.

The following chapter will employ the theoretical background presented in the current chapter to define the initial and boundary conditions for the project while also showcasing the implementation of radiative cooling within the simulation framework. Additionally, the software and the computational tools employed in this study will be introduced, which were chosen based on their suitability to perform wind-multicloud simulations.

Chapter 3

Methodology

3.1 Software

To study wind-multicloud systems, we resort to numerical simulations in which a supersonic wind interacts with a group of clouds separated by different distances. For this purpose, we utilise a set of computational tools, initial conditions, and numerical diagnostics which are described below.

3.1.1 The PLUTO Code

PLUTO*, created by Mignone et al. (2007)[44], is a free and open-source package of numerical solvers. This package includes a set of modern numerical algorithms designed for solving systems of hyperbolic and parabolic partial differential equations that are relevant for astrophysical gas dynamics. The code can be adapted to solve the Euler or Navier-Stokes equations using either finite-difference or finite-volume techniques based on Godunov-type schemes. AGN jets, molecular clouds, galactic winds, and stellar winds are only a few of the astrophysical phenomena whose evolution this package has successfully simulated. We have used the PLUTO code to numerically solve the mass, momentum, and energy conservation equations of ideal hydrodynamics due to its adaptability, numerical stability, and robust nature. The code, which is written in the C programming language and contains a python-wrapping interface, can run on a range of computing systems, from a single workstation to high-performance computing facilities containing thousands of processors. It does so by utilizing the Message Passing Interface (MPI) to achieve multi-core parallelisation (on CPU-based architectures) and optimal performance and resolution.

3.1.2 Python

Python is a high-level programming language that is widely used in data analysis and scientific computing. We employ Python to read in and analyse the TB-sized datasets that come from our simulations. This language is an adequate tool for these jobs because of its flexibility of use, adaptability, and large module library. Python additionally allows us to create scripts that automate repetitive operations, improving the effectiveness of our workflow. Additionally, we are able to create informative plots and animations that provide insights on the dynamics of astrophysical media thanks to Python's state-of-the-art data visualization packages. The ability to link Python interfaces with other software tools such as PLUTO enables us to do more sophisticated numerical analyses on the simulation data.

---

*http://plutocode.ph.unito.it/

3.1.3 Computational requirements

To perform the simulations described in the subsequent section, it is necessary to have access to high-performance computing resources. Running these simulations at the desired resolution and time requires the use of multiple-processor CPU-based architectures and parallel domain decomposition with the Message Passing Interface (MPI) library. The simulations presented in this thesis were conducted on the high-performance computing (HPC) facility SuperMUC-NG, which is operated by the Leibniz Supercomputing Centre (LRZ) in Germany. The SuperMUC-NG system is equipped with a total of 311,040 Intel Skylake Xeon CPUs that provide a peak performance of 26.9 PetaFlops/s[†].

The parallelized computation for the three-dimensional simulations requires between 1024 - 1920 cores (CPUs) depending on the desired resolution. The computation cost varies according to the resolution: low-resolution simulations have a cost of $\sim$ 150 SU[*], standard resolution simulations have a cost of $\sim$ 1.5 kSU, while high-resolution simulations have a cost of $\sim$ 15 kSU. The analysis of the simulation results was conducted using single-processor Python routines, which were independent of one another and required a computational cost of $\sim 1-10$ SU, depending on the resolution of the data set analyzed (see Table 3.1). To store the output files, which included plots, data files, and simulation data, we need $\sim$ 10 TB. This data was stored in several locations, including the HPC facility, a cloud storage service, and a personal computer.

3.2 Simulation Set-up

3.2.1 Wind-multicloud Simulations

The investigation of the changes in cold clouds as a result of their interactions with galactic winds was conducted using the PLUTO v4.4 code (Mignone et al. 2007[44]). The simulations were carried out by simultaneously solving the ideal hydrodynamic (HD) equations in a three-dimensional Cartesian coordinate system (X, Y, Z). The mass, momentum, and energy conservation laws are:

$$\frac{\partial \rho}{\partial t} + \nabla \cdot [\rho \boldsymbol{v}] = 0, \tag{3.1}$$

$$\frac{\partial [\rho \boldsymbol{v}]}{\partial t} + \nabla \cdot [\rho \boldsymbol{v}\boldsymbol{v} + \boldsymbol{I}P] = 0, \tag{3.2}$$

[†] `www.lrz.de`

[*] 1 SU = 1 Service Unit = 1 CPU-hour

$$\frac{\partial E}{\partial t} + \nabla \cdot [(E + P)\boldsymbol{v})] = \Lambda, \tag{3.3}$$

where $\rho = \mu m_u n$ is the mass density, μ is the mean particle mass, m_u is the atomic mass unit, n is the gas number density, $\boldsymbol{v}$ is the velocity, and Λ is the volumetric cooling rate. The ideal equation of state used for the astrophysical gas is given by:

$$P = (\gamma + 1)\rho\epsilon, \tag{3.4}$$

Here, ϵ represents the specific internal energy of the gas. The value of the polytropic index γ is set to $\frac{5}{3}$ for both adiabatic and radiative simulations. In addition, we include the additional advection equation of the form:

$$\frac{\partial \rho \boldsymbol{C}}{\partial t} + \nabla \cdot [\rho \boldsymbol{C} \boldsymbol{v}] = 0, \tag{3.5}$$

where C is the Lagrangian scalar, which we used to track the evolution of gas initially contained in the cloud material, defined as $C = 1$ for the gas inside the multi-cloud system and $C = 0$ everywhere else.

In order to solve the system of hyperbolic conservation laws described above, the PLUTO code was configured to use the HLLC approximate Riemann solver as proposed by Toro, Spruce, and Speares (1994)[45]. The HLLC solver is an extension of the HLL Riemann solver that takes into account the pressure discontinuity at the contact wave, thereby improving its accuracy. Compared to the HLL solver, the HLLC solver provides a more precise representation of the flow across the contact wave, resulting in better resolution of shocks and contact discontinuities. The time marching algorithm used for this work is Runge-Kutta third-order method (RK3) as it provides a good balance between accuracy and computational cost. The aforementioned combined with the piecewise parabolic method (PPM) of spatial reconstruction offers an accurate capture of shocks and discontinuities, especially in compressible flows (see Mignone 2014[46]). Finally, to ensure the stability of the numerical simulations, we set the Courant-Friedrichs-Lewy (CFL) number to 0.33. The CFL limit for the simulation to remain stable is given by PLUTO conditions for different time stepping methods (see Mignone 2014[46]). In the case of RK3, the limit can be inferred by CFL $\lesssim 1/\mathrm{N}_{dim}$ where N_{dim} is the number of spatial dimensions.

3.2.2 Initial and Boundary Conditions

Our study involves the simulation of a two-phase ISM composed of spherical cold clouds surrounded by a hot supersonic wind with a uniform velocity distribution. For the purpose of this study, we employed the analytical model of a hot wind based on the adiabatic CC85 model explained in Section 2.1 (see Figure 2.1). To determine the input parameters for the derived CC85 model, we referred to the fits obtained by Strickland & Heckman (2009)[30] of the nearby starburst galaxy M82. We have restricted our attention to the supersonic wind region: thus, we use the CC85 solution for $r > R$ (see Equation (2.5) and Figure 2.1). For the specified α, β, M_{hot}, and R of M82, the CC85 solutions (see Equations (2.6) to (2.16)) provides velocity, density, and temperature of the hot wind.

The simulation domain is a rectangular prism with a (1:4:1) aspect ratio for the (W, L, H) domain where the width, length, and height of the prism are denoted as W, L, and H, respectively. To preserve all of the cloud material, periodic boundary conditions are included in the simulation as follows:

$$f(x_{beg}, y, z) = f(x_{end}, y, z), \qquad \text{for} \quad 0 \leq x \leq \mathrm{W}, \tag{3.6}$$

$$f(x, y_{beg}, z) = f(x, y_{end}, z), \qquad \text{for} \quad 0 \leq y \leq \mathrm{L}, \tag{3.7}$$

$$f(x, y, z_{beg}) = f(x, y, z_{end}), \qquad \text{for} \quad 0 \leq z \leq \mathrm{H}. \tag{3.8}$$

We arranged a series of perfectly ordered clouds along Y (which is the streaming direction). We place clouds at different separation distances using a range of δ values, which cover values from 2 to 64 (see Section 2.3 for the definition of δ). The clouds are placed along the Y-axis at the centre of the XZ plane. The Y-axis therefore acts as the direction of relative motion between the clouds and the background wind. Each of these cold clouds is initially static and characterized by a uniform density distribution, with a radius equivalent to 6.25% of the X- or Z-size of the box (see Figure 3.1).

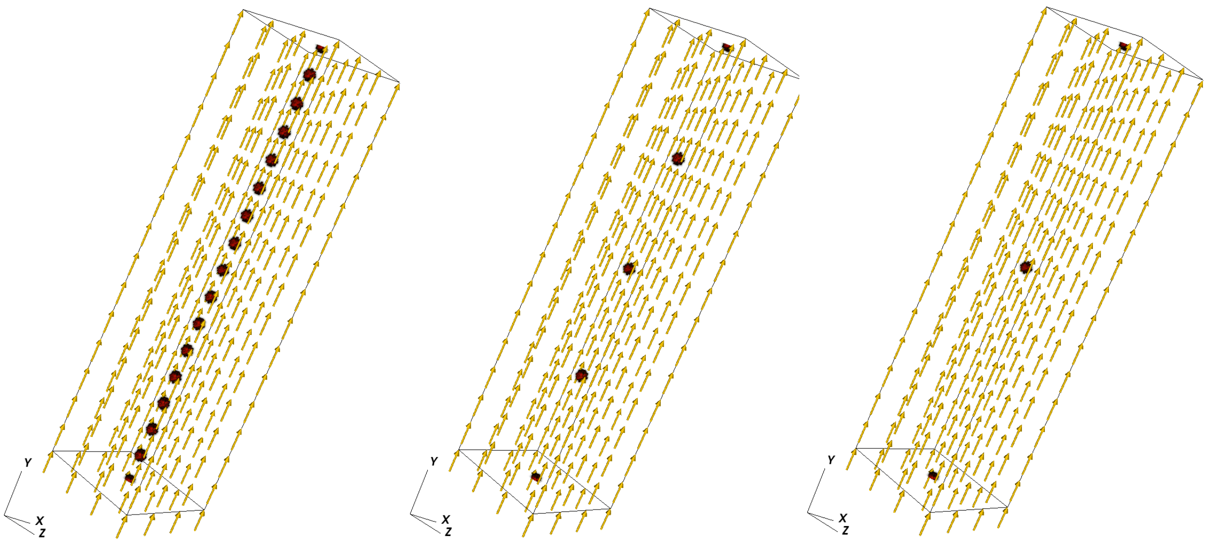
(a) $\delta = 4$ (b) $\delta = 16$ (c) $\delta = 32$

Figure 3.1: Three-dimensional setup of our wind-multicloud models featuring the initial positions of a collection of spherical clouds, each separated from one another by a uniform distance of $\delta = 4$, $\delta = 16$, and $\delta = 32$ respectively. In addition, arrows illustrate the uniform velocity field that represents the galactic wind.

This research primarily focuses on the study of gas phases with temperatures between $\mathrm{T} \sim 10^4 - 10^8$ K. Gas at these temperatures is generally optically thin, which means that the gas does not drastically absorb or scatter light[42]. This property makes it easier to observe and measure the characteristics of the gas through observations in various spectral ranges, including ultraviolet (UV), optical, and X-ray wavelengths. Moreover, Wiersma et al. (2009)[42] pointed out that the influence of photoionization is typically less relevant at higher temperatures. Therefore, the simulations include radiative cooling from atomic species in a temperature range spanning from $10^4 - 10^9$ K (see Section 2.4). We used the tabulated cooling function data precalculated with the CLOUDY (version 07.02 2009) package[‡] by Wiersma et al. (2009)[42]. The normalized, net cooling rate ($\left|\Lambda/n_H^2\right|$) is illustrated in Figure 3.2 as a function of temperature. Moreover, we introduce a cooling floor threshold at 10^4K, which is considered to mimic the effects of radiative heating, which dominates the thermal evolution of gas below that temperature. Therefore, gas with temperatures below the cooling floor 10^4K will not be able to continue cooling.

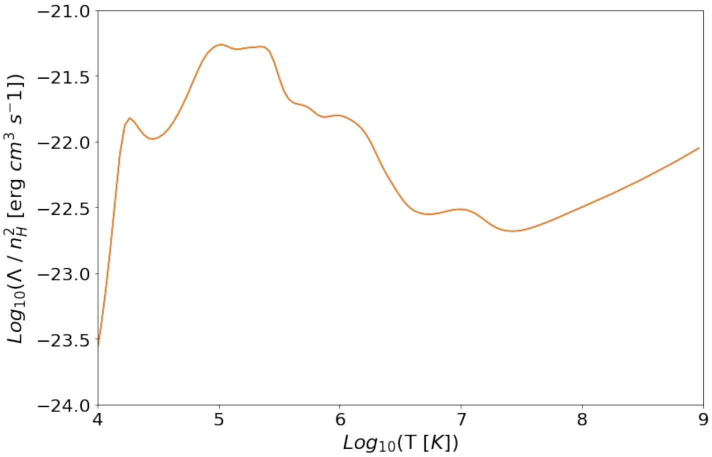

Figure 3.2: Net cooling rate ($|\Lambda/n_\mathrm{H}^2|$), normalized and expressed in absolute terms as a function of gas temperature

This study comprises a total of 20 numerical simulations aimed at investigating the impact of hydrodynamic shielding in a multicloud gas stream (see Table 3.1). The simulations were run for a duration of t ~ 5 Myr or t_cross = 400. The first part of the study (presented in Section 4.1) involved two adiabatic and radiative numerical simulations which allowed us to examine the effects of a supersonic hot wind interacting with cold clouds and to study the effect of radiative cooling. The second part (presented in Section 4.2) comprises 10 adiabatic and radiative numerical simulations, in which we have studied the effects of hydrodynamic shielding and how the separation value δ influences the evolution of cold clouds. In the last part of the study (see Section 4.3), we conducted eight adiabatic and radiative simulations of both higher and lower resolutions to study the numerical convergence of both models.

3.3 Diagnostics

To study the evolution of a set of clouds in a wind-multicloud model, several diagnostics can be calculated from the simulated data. The mass-weighted volume average of the variable $\mathcal{G}$ can be computed by:

$$\langle\mathcal{G}\rangle = \frac{\int \mathcal{G}\rho C dV}{M_{cl}} = \frac{\int \mathcal{G}\rho C dV}{\int \rho C dV}, \tag{3.9}$$

[‡] `http://www.nublado.org/`

Table 3.1: Overview of the simulation parameters chosen for different models. Columns 1 and 2 respectively indicate the type of thermodynamic model introduced for the simulation and the resolution in units of X (number of cells per cloud radius with the standard notation, R_x). Columns 3 and 4 indicate the number of cells in the 3D domain and the density contrast between the clouds and the wind. Columns 5 and 6 indicate the cooling floor and the distance between clouds given by the dimensionless parameter δ (see Section 2.3 for the definition).

Model	Resolution	Number of cells	χ	$\mathcal{M}_{wind}$	Cooling floor	δ
Adiabatic	R_{16}	$(256 \times 1024 \times 256)$	10^2	3.5	-	2, 4, 8, 16, 32, 64
Radiative	R_{16}	$(256 \times 1024 \times 256)$	10^2	3.5	10^4	2, 4, 8, 16, 32, 64
Adiabatic	R_{32}	$(512 \times 2048 \times 512)$	10^2	3.5	-	8, 16
Adiabatic	R_8	$(128 \times 512 \times 128)$	10^2	3.5	-	8, 16
Radiative	R_{32}	$(512 \times 2048 \times 512)$	10^2	3.5	10^4	8, 16
Radiative	R_8	$(128 \times 512 \times 128)$	10^2	3.5	10^4	8, 16

where V is the volume, C is the tracer of the cloud material, and M_{cl} is the cloud mass as a function of time. In a similar way, the volume-averaged value of the variable $\mathcal{F}$ is given by:

$$[\mathcal{F}] = \frac{\int \mathcal{F} C dV}{V_{cl}} = \frac{\int \mathcal{F} C dV}{\int C dV}, \tag{3.10}$$

where V_{cl} is the total cloud volume as a function of time. The degree of mixing between the cloud and the surrounding wind is defined as:

$$f_{mix} = \frac{\int \rho C^* dV}{M_{cl,0}}, \tag{3.11}$$

where the numerator represents the mass of mixed gas with $0.01 < C^* < 0.99$, and $M_{cl,0}$ represents the mass of the cloud material at time $t = 0$. Additionally, we define the dense gas mass fraction (Heyer et al. 2022[47]) as the ratio of cloud mass with a density greater than a threshold density ρ' to the total cloud mass:

$$f_{DG}(\rho > \rho') = \frac{M(\rho > \rho')}{M_{Tot}}, \tag{3.12}$$

where ρ' is chosen based on the specific type of dense gas of interest. For this work, we are going to consider $\rho' = 0.5 \times \rho_{cl,0}$ to focus on the cloud material that has more than half the density of the initial density value of the cloud. The mass of cold gas is determined by considering the mass of material with a temperature below $10T_{cl,0}$, where $T_{cl,0}$ represents the initial temperature of the cold gas.

$$M_c = \frac{M(10T_c > T)}{M_{Tot}}, \tag{3.13}$$

this corresponds to a temperature logarithmically halfway between the initial temperatures of the cold and hot media (Forbes et al. 2019[20]) since the simulation is initialized in thermal pressure equilibrium with a density contrast of $\chi = 10^2$.

This chapter has provided a thorough overview of the methodology employed in this project, encompassing the introduction of the necessary computational tools and initial conditions essential for conducting the wind-multicloud simulations. In the upcoming chapter, we will present the outcomes obtained from the simulations along with a comprehensive discussion and analysis of the results.

Chapter 4

Results & Discussion

4.1 Global evolution

This and the following sections provide a detailed account of the global interaction between a hot supersonic wind and a multi-cloud system.

4.1.1 Evolution of a wind-multicloud system

Figures 4.1, 4.2, and 4.3 display two-dimensional slices at Z = 0 of the gas temperature, pressure, and number density, respectively. These panels correspond to our control adiabatic and radiative models with the standard separation $\delta = 16$. The choice of the standard separation value, $\delta = 16$, was motivated by its position as an intermediate value within the range of separation values considered. The overall evolution of this particular pair of models, which is also relevant for the others, can be characterized by the following stages:

- In the first stage (see Fig 4.1b, 4.2b, and 4.3b), the impact of the wind material on the front surface of the clouds produces internal shock within the clouds of the multi-cloud system. The internal refracted shocks are accompanied by external reflected shocks, which travel upstream. The reflected shocks create bow shocks at the leading edge of the clouds, while the refracted shocks travel through the clouds. Due to pressure gradient forces and shock heating, the clouds accelerate and expand, stretching upstream. As the clouds expand, they undergo a steady disruption, resulting in the formation of filamentary tails of cloud material. Moreover, the simulations show the formation of turbulent wakes downstream from each cloud which exhibit intermediate densities and temperatures.
- In the second stage (see Fig 4.1c, 4.2c, and 4.3c), as the multi-cloud system interacts with the incoming wind, a bow shock is formed at the front surface of clouds. However, the strength of the bow shock decreases over time as the momentum transfer between the wind and the cloud takes place and results in cloud acceleration. As a mixture of upstream wind and cloud material continues to flow downstream, it envelops the other clouds,

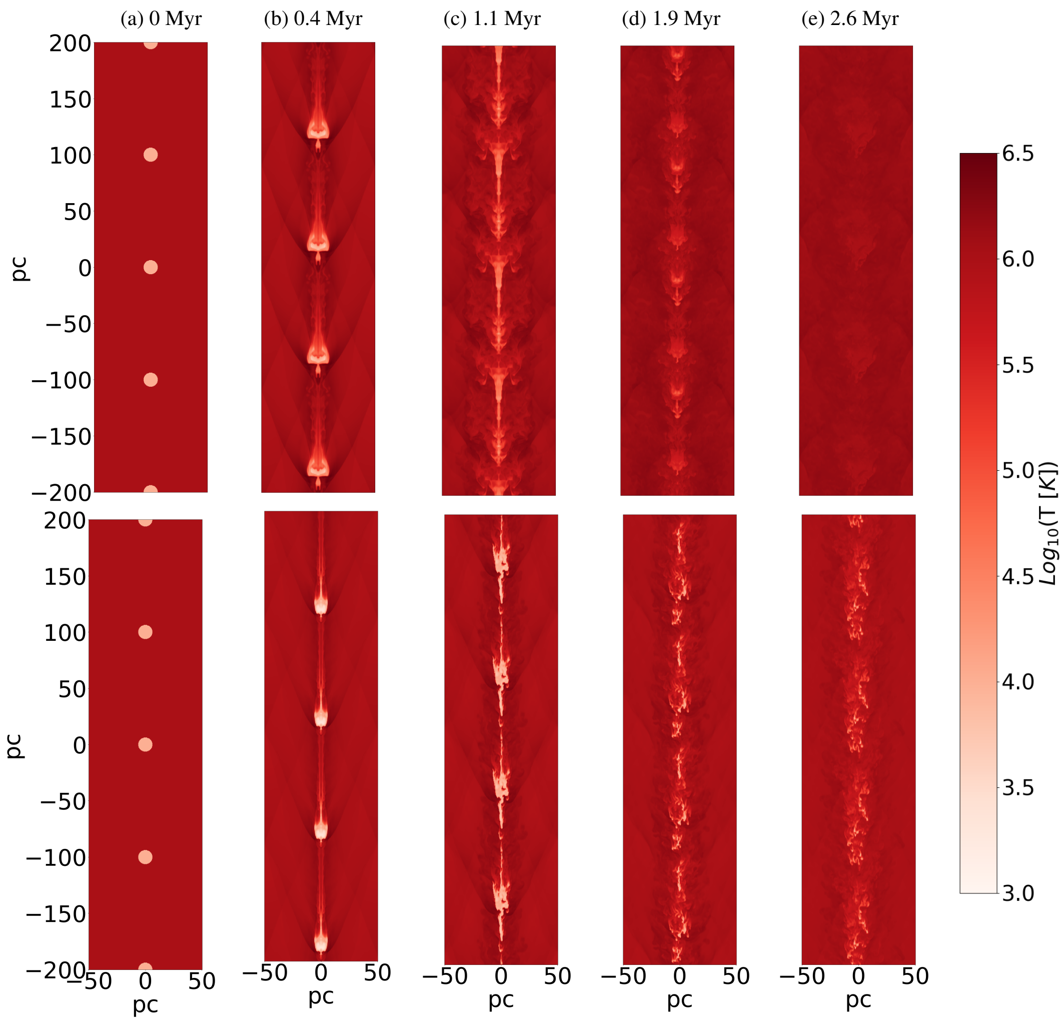

Figure 4.1: Two-dimensional slices at Z = 0 of the temperature in the adiabatic (top) and radiative (bottom) models at five different times through the simulation (columns).

providing shielding from the hot background. However, the clouds also start to lose mass via stripping caused by KH instabilities from their surface layers. The growth time of KH instabilities on HD models depends mainly on the density contrast between both media, χ, and the relative velocity at the boundary layer, $(v'_w - v'_c)$. In this case, the KH instabilities occur primarily at the sides of the clouds, where higher relative velocity shears exist. The swirling vortical motion associated with KH instabilities removes cloud material, which is carried upstream leading to the mixing of wind and cloud material. The disruption process also forms long streamers of stripped gas that extend downstream.

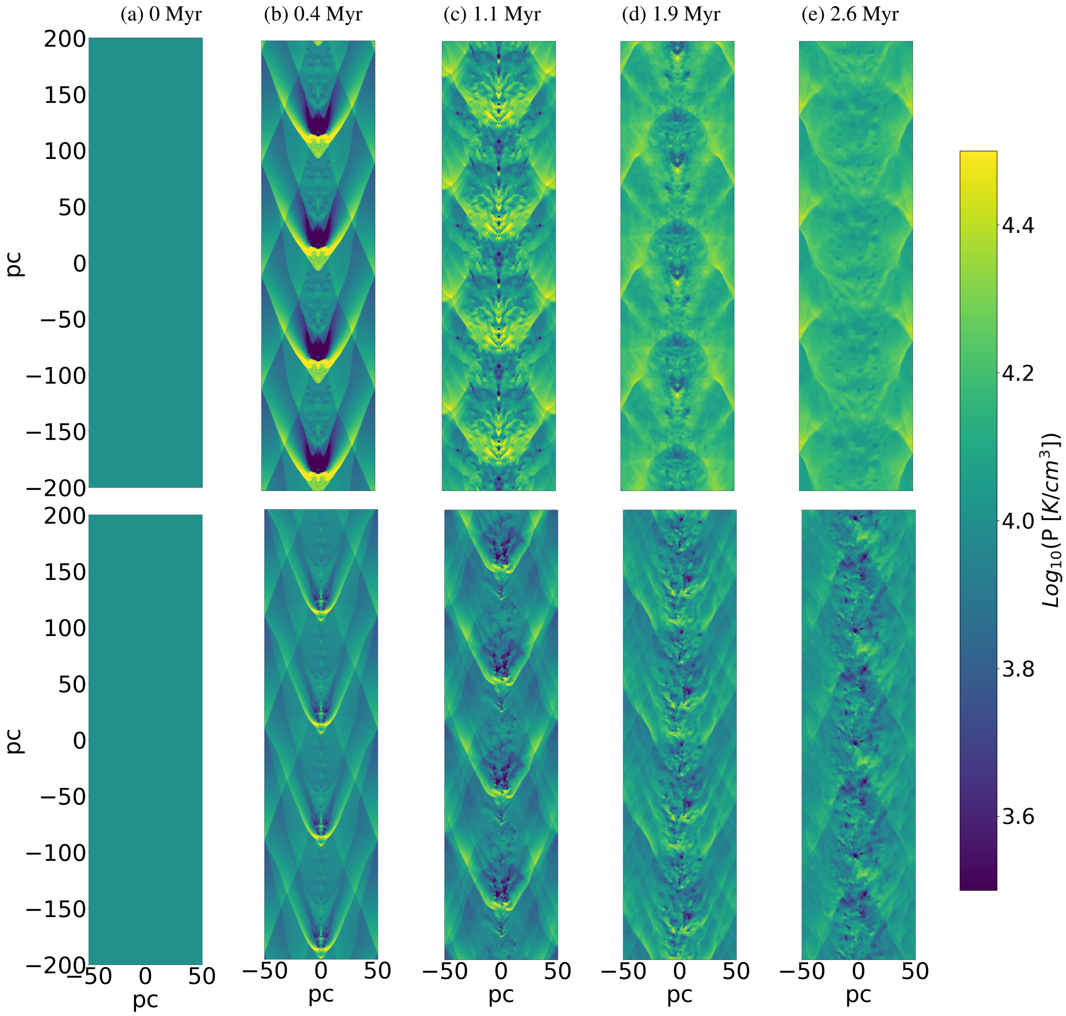

Figure 4.2: Two-dimensional slices at Z = 0 of the thermal pressure in units of P/k_b in the adiabatic (top) and radiative (bottom) models at five different times through the simulation (columns).

- In the third stage (see Fig 4.1d, 4.2d, and 4.3d), the downstream motion of the wind triggers the collision between the filamentary tails of the upstream clouds (the clouds that are near the bottom of the simulation domain) with the cloud cores of the downstream clouds (the clouds that are near the top of the simulation domain). This interaction plays a crucial role in preserving the structural integrity of the cloud cores, as the clouds can effectively shield and mitigate the disruptive effects caused by drag forces and Rayleigh-Taylor (RT) instabilities, providing a significant level of protection against these effects. As the clouds move downstream,

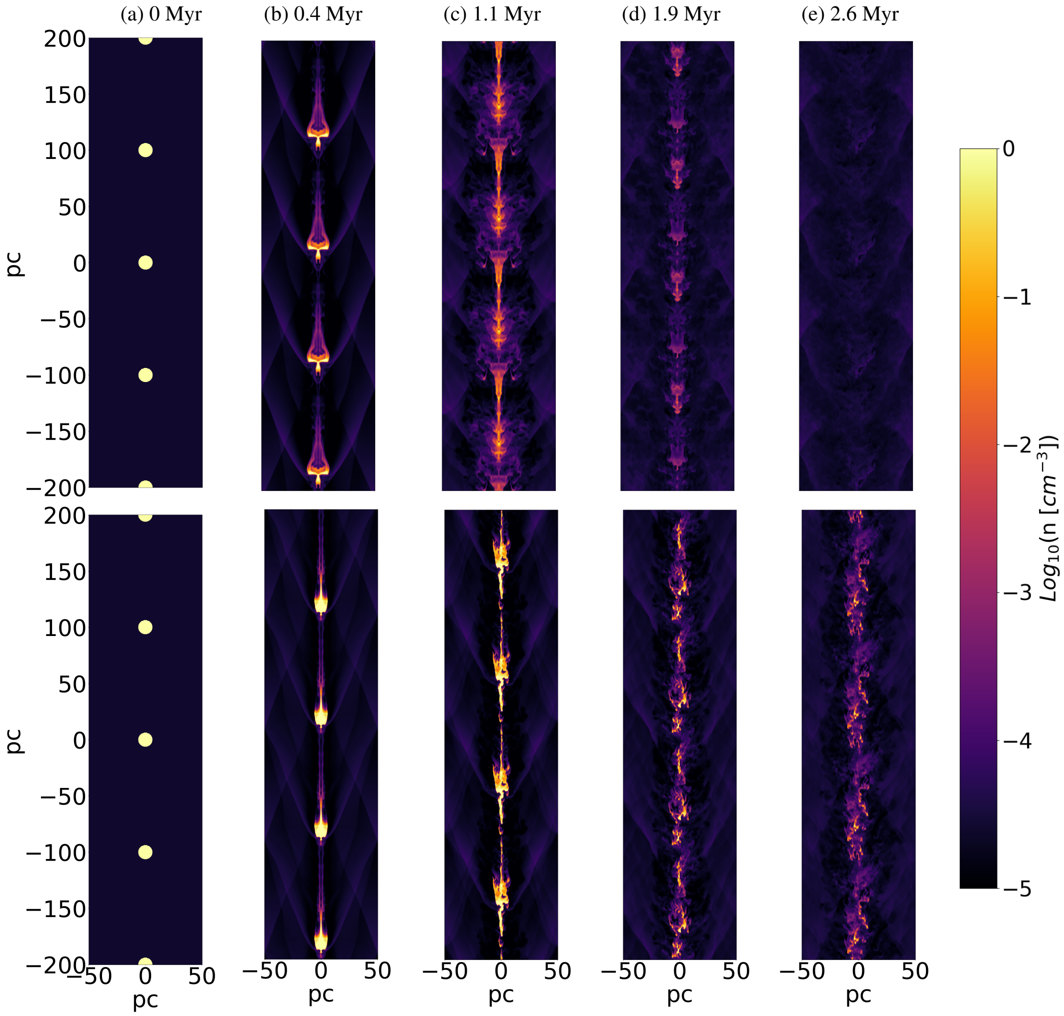

Figure 4.3: Two-dimensional slices at Z = 0 of the number density in the adiabatic (top) and radiative (bottom) models at five different times through the simulation (columns).

the KH instabilities cause further stripping of their outer layers. Nonetheless, the degree of mass loss is non-uniform across the cloud, with the outside layers being more susceptible to mass loss than more internal layers. Meanwhile, as the boundary conditions are periodic along Y, turbulent wakes of the downstream clouds can also collide with the turbulent wake material of the upstream clouds. This collision enhances the creation of a long gas stream of hot and dense material, further complicating the dynamics of the system.

- In the final stage (see Fig 4.1e, 4.2e, and 4.3e), the clouds have undergone substantial mass loss as a result of hydrodynamic shredding. Additionally, their acceleration has reached a level that is conducive to the growth of RT instabilities. The RT instabilities favour the formation of low-density wind gas bubbles and high-density spikes of cloud material at the front of each cloud. As the cross-sectional area increases, RT instabilities grow, which results in the disruption of the main cloud cores, which break up into smaller cloudlets. While some of these cloudlets eventually dissolve into the background medium, others acquire the full wind speed. Ultimately, it is RT perturbations that cause the destruction of clouds. In fact, low-density bubbles rapidly penetrate the denser layers of the clouds, causing disruption to the remaining cloud filaments. The remaining clouds then shatter into several cloudlets, which expand and mix further with the ambient gas. This process represents the final stage of cloud shredding and ultimately results in the complete destruction of the clouds.

It is important to remark that the break-up process can be accelerated or decelerated, depending on the inclusion or not of radiative cooling and the initial separation distance, δ, of the clouds. In the next subsection, we see a detailed comparison between adiabatic and radiative models, and we present a detailed account of how instabilities develop under different separation values δ, and how they affect the morphology of the resulting filaments and cloudlets.

4.1.2 The Role of Radiative Cooling

The bottom rows of Figures 4.1, 4.2, and 4.3 illustrate the evolution of wind-multicloud models with the inclusion of radiative cooling. Comparing the two models, it is apparent that their evolution begins almost identically. A bow shock is formed as the wind interacts with the front surface of each cloud. In the adiabatic model, the shock produced from the interaction between the wind and the clouds results in the compression of the cloud and the subsequent injection of thermal energy. This energy is then converted into heat, which not only increases the temperature of the cloud but also contributes to the expansion and mixing of the cloud gas with the wind gas. Therefore, without an efficient mechanism of energy dissipation, the cold gas is eventually heated and disrupted by instabilities.

In contrast, the inclusion of radiative cooling leads to significant changes in the behaviour and morphology of the clouds. The efficient cooling process removes the aforementioned thermal energy (injected by internal shocks) that would have been otherwise converted into heat. This prevents the pronounced increase in thermal pressure characteristic of adiabatic models (see Fig 4.2e). Instead, cooling-induced pressure gradients foster turbulence and promote the mixing of wind gas and cloud gas. Moreover, radiative cooling produces denser clouds where the cooled gas remains protected from instabilities, enveloped by a warm ($T \sim 10^{4.5}$K) radiative layer of mixed, medium-density gas. As a result, the most significant effect of the inclusion of radiative cooling is that the clouds exhibit a longer lifetime.

4.1.3 Thermodynamic Evolution of the Cloud Gas

Figure 4.4 shows the time evolution of mass-weighted phase diagrams of temperature versus number density of cloud material for both adiabatic and radiative systems. In the adiabatic model, the cloud material experiences rapid heating, with the majority of the material reaching temperatures $T > 10^4$K. Due to the absence of mechanisms to release the extra energy injected via shocks, the cold gas is heated up and then shredded by instabilities leading to a lack of dense cloud material at low temperatures. By t = 2.1 Myr, most of the cloud mass corresponds to hot gas with temperatures T > 10^5 K which has already expanded transversely (i.e. along the X and Z directions). Finally, by t = 3.8 Myr, all the cloud mass is composed of gas with temperatures T > 10^6K and number densities n ~ 0.01cm^{-3}, conditions that we normally associate with X-ray emitting gas.

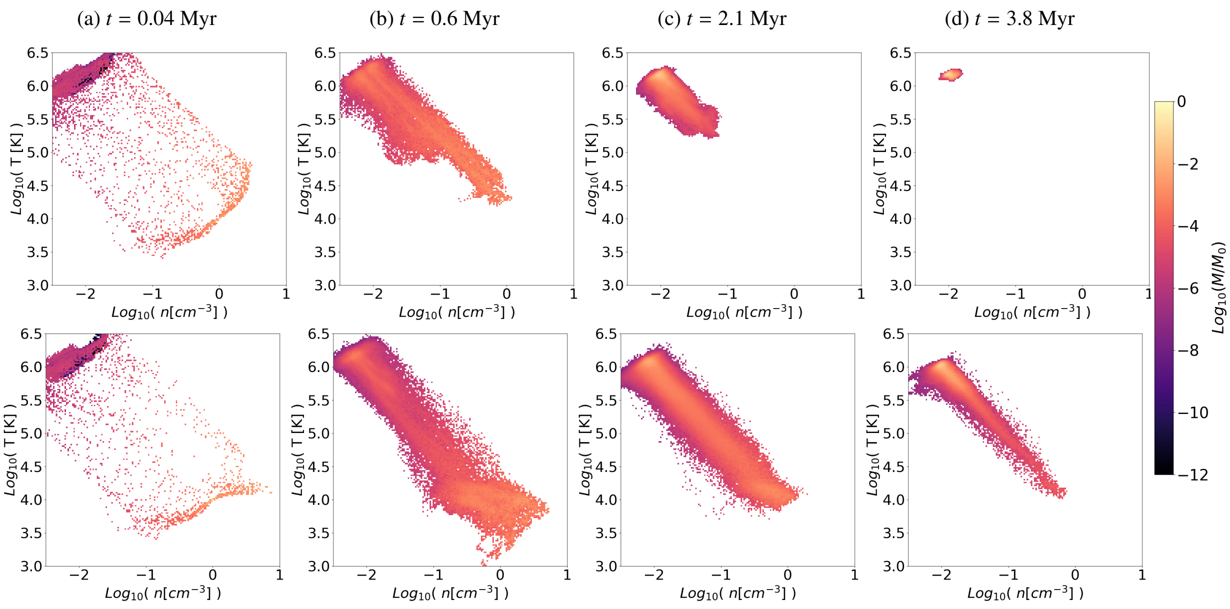
(a) t = 0.04 Myr
(b) t = 0.6 Myr
(c) t = 2.1 Myr
(d) t = 3.8 Myr

Figure 4.4: Mass-weighted phase diagrams displaying the two-dimensional distributions of temperature and density of cloud material in the adiabatic (top) and radiative (bottom) δ = 16 model.

The radiative model exhibits a different thermodynamic evolution of cloud gas. In the early stages of the simulation (t = 0.6 Myr), downstream cloud gas undergoes cooling, while the gas pushed upstream by the wind is initially heated up. The unshocked cloud gas at the core of each cloud gradually cools down to temperatures T ~ 10^4K. This results in a slower heating rate of the gas compared to the adiabatic case, which leads to geometrically thinner tails of cloud material, compared to the adiabatic cases. During most of the simulation time, two distinct gas phases are observed, characterized by a cooler and denser phase with T ~ 10^4K and n ~ 1cm^3, and a lower-density and higher-temperature phase with T ~ 10^6K and n ~ 0.01cm^3. The overall flow is therefore multi-phase, and resembles much more the observed structure of galactic winds.

Figure 4.5 shows the time evolution of the mass-weighted average temperature (see equation 3.9), the mean density (see equation 3.10), and the dense gas mass fraction (see equation 3.12), off all cloud material, in both the adiabatic and radiative models. In the absence of radiative cooling, the adiabatic wind-multicloud system manages to maintain its dense gas mass only until t ~ 1.2 Myr while the radiative model still maintains 60% of dense material over the same time-scale. Eventually, at the end of the simulation time, both models lose all the dense material but it is important to note that the radiative model prolongs the lifetime of dense gas at least three times (up to t $\sim$ 3.5 Myr) compared to the adiabatic model. As cloud gas continues interacting with upstream clouds and the wind, it continues mixing, producing denser gas with temperatures $T < 10^5$K. This denser gas is also subjected to erosion and heating but can overall slow down this trend and cool. As a result, not all the gas will be heated to temperatures $\gtrsim 10^6$ K by the end of the simulation time. Therefore, radiative cooling allows for the continuous replacement of dense gas in the outflow which maintains temperatures lower than the surrounding ambient temperature.

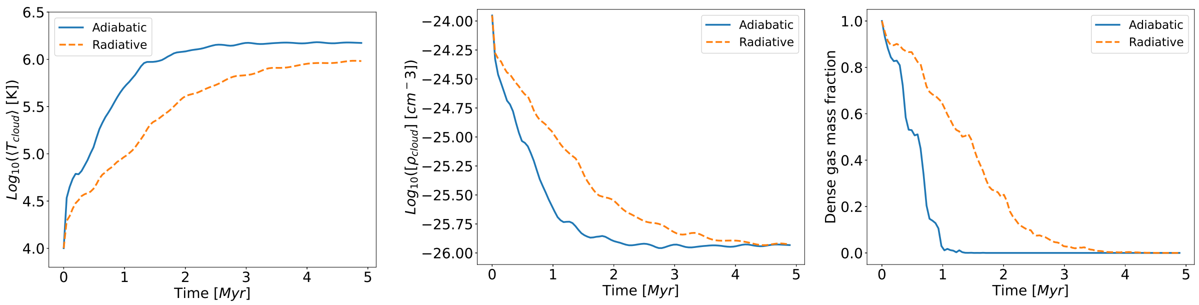
(a) Mass-weighted average temperature

(b) Mean density

(c) Dense gas mass fraction

Figure 4.5: Time evolution of the mass-weighted average temperature (left panel), mean density (middle panel), and dense gas mass fraction (right panel) of cloud material in both the adiabatic and radiative $\delta = 16$ model.

4.1.4 Cloud Dynamics and Survival

The dynamical evolution of the clouds in both $\delta = 16$ models occurs in different ways by using some of the diagnostics defined in Section 3.3. Therefore, there is the necessity of quantifying their differences. Figure 4.6 depicts the mixing fraction between the gas and the cloud material (see equation 3.11), the cold gas mass fraction (see equation 3.13), and the mass-weighted average velocity (see equation 3.9) in cloud material for the adiabatic and radiative $\delta = 16$ models. Adiabatic models exhibit a high degree of turbulence, which leads to mixing with the background medium. The mixing and dispersion processes are associated with the generation of vortical motions via KH instabilities and the high pressure exerted on the clouds. As a result, the edges of the clouds are stripped of material, and a tail is formed downstream of each cloud. In the adiabatic model, the continuous expansion of the clouds leads to the formation of a geometrically thick tail downstream of each cloud. The continuous expansion not only heats up the material but also triggers its destruction in regions where the density is low.

On the other hand, the cloud material in radiative models is able to survive since the growth of KH instabilities is delayed owing to the larger density contrasts that emerge when we consider radiative cooling. In radiative models, the expansion of the clouds decreases, which results in the formation of a thin tail behind the clouds. This mechanism enhances the formation of small gas clumps and fragments of clouds, resulting in a denser medium. This denser medium provides protection for cloud material, which now occupies a smaller volume. However, the time evolution

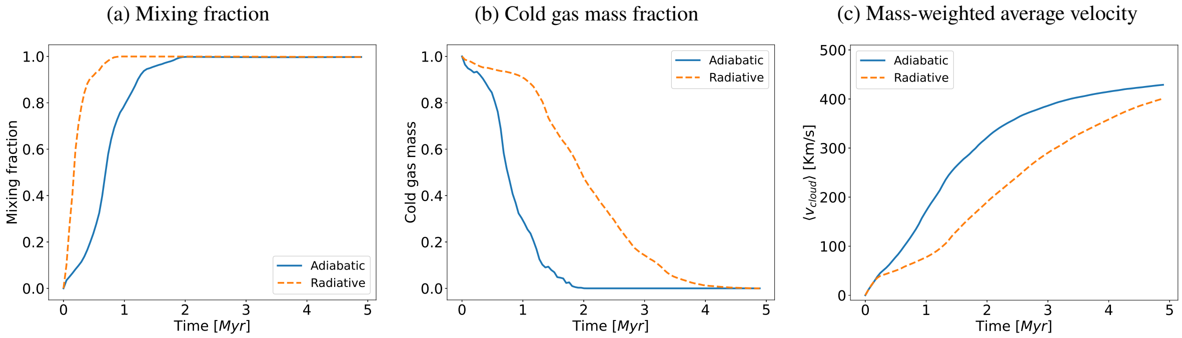
(a) Mixing fraction (b) Cold gas mass fraction (c) Mass-weighted average velocity

Figure 4.6: Time evolution of the mixing fraction, cold gas mass fraction, and mass-weighted average velocity of cloud material in the adiabatic and radiative $\delta = 16$ models.

of the mixing fraction (see Figure 4.6) suggests that radiative models exhibit a higher degree of mixing compared to adiabatic models. This occurs because, in adiabatic models, mixing arises only due to the growth of KH and RT instabilities over time, while radiative models, in addition to instabilities, generate additional mixing due to cooling-induced pressure gradients and condensation. Condensation occurs at the early stages of the radiative models, where warm gas with T$\sim 10^{4.5} - 10^{5.5}$K efficiently condenses into colder and denser material as the cooling rates (see Fig. 3.2) peak at those temperatures. In general, the high degree of mixing at early stages in radiative models occurs due to the efficiency of cooling of warm material that condenses back into cold gas, whereas, in the adiabatic model, the mixing arises due to the growth of KH and RT instabilities.

The analysis of the cold gas mass fraction shows that the radiative model preserves cold material (for which $10\mathrm{T}_c > \mathrm{T}$) for a significantly longer period compared to the adiabatic model. This occurs as a result of the presence of shocked cloud material that has already mixed and can condense back into a colder and denser phase. Therefore, these cloud components gradually disperse throughout the outflow and collide with the cold material of downstream clouds.

The velocities of the adiabatic clouds are generally higher compared to the radiative ones. In contrast, radiative models are characterized by efficient cooling of the warm, mixed gas, which leads to the presence of more dense gas. Such gas with higher column densities is more difficult to accelerate via direct momentum transfer (see Banda-Barragan et al. 2021[48]). Thus, the expansion of adiabatic clouds results in a higher rate of acceleration. The warm gas (T $\sim 10^5$K) in them keeps accelerating and heating up, whereas, in the radiative model, the warm gas condenses back into the cold phase while it expands upstream. Although there is no direct momentum transfer to the radiative clouds, the gas that condenses back into the cold phase preserves some of the momentum that was present in the warm phase (see discussion in Schneider et al. 2020[49]).

4.2 Hydrodynamic Shielding

In this section, we discuss the impact of having clouds perfectly aligned upstream and downstream of each other, and how this can affect the morphology and longevity of cloud material as a result of hydrodynamic shielding. Additionally, we also compare the dynamic and thermodynamic differences that occur when we adjust the cloud separation distance, δ.

4.2.1 The Role of Hydrodynamic Shielding

In the previous section, we presented various numerical analyses for both adiabatic and radiative models showcasing differences and similarities between adiabatic and radiative clouds.

The arrangement of clouds in a stream-like formation affects how they interact with the surrounding environment compared to isolated cloud formations. In general, clouds in streams have a greater capacity to shield themselves from disruption caused by the interaction with low-density supersonic gas. The interaction between clouds is a result of the displacement induced by the supersonic wind. As previously observed, the morphology of downstream clouds is not solely influenced by the background, but also by the upstream clouds that eventually collide, altering their morphology and physical properties. Generally, cloud material subjected to hydrodynamic shielding can persist for longer periods due to its ability to survive dynamic shredding and drag.

The filaments created from the stripping of the outer layers of the clouds, as a result of instabilities, serve as a protective cover for the downstream cloud cores once they reach them (e.g. Figure 4.7b and Figure 4.9b). As the wind continues to flow downstream, it also interacts with downward clouds which means that part of the gas that already directly interacted with the preceding cloud, starts to interact with downstream clouds. This means that the evolution of the individual clouds along the gas stream is not independent, but relies on the interaction between the hot wind, the other clouds further upstream, and mixed gas that has already interacted with upstream cold material.

4.2.2 On the effects of the separation distance, δ, between clouds

In this section, we will explore the effects of changing the separation distance, δ, between the clouds along the stream. Figure 4.7, 4.8, 4.9, and 4.10 show two-dimensional slices of the number density for several separation distances, ranging from $\delta = 2$ to $\delta = 64$. The effects of placing a group of cold clouds interacting with a hot background medium can vary widely. For instance, those clouds, separated by large distances (i.e. high δ values), that are unable to withstand the hydrodynamic drag forces will completely disintegrate and mix with the surrounding medium at a very fast pace. In contrast, we show in this thesis that a group of clouds can form a multiphase medium where there is continuous condensation allowing for the preservation of a large fraction of dense gas.

The most obvious trend observed in the figures is that reducing the separation value between clouds results in a substantial increase in hydrodynamic shielding, which in general helps preserve the material of the cool cloud for a longer period of time. The frequent interaction between clouds causes the cold material to be shielded by a layer of disrupted warm material from the upstream clouds, which reduces the effective drag forces acting on downstream clouds. Thus, closely-spaced clouds can effectively act as a cylindrical-like stream of cold material. Alternatively,

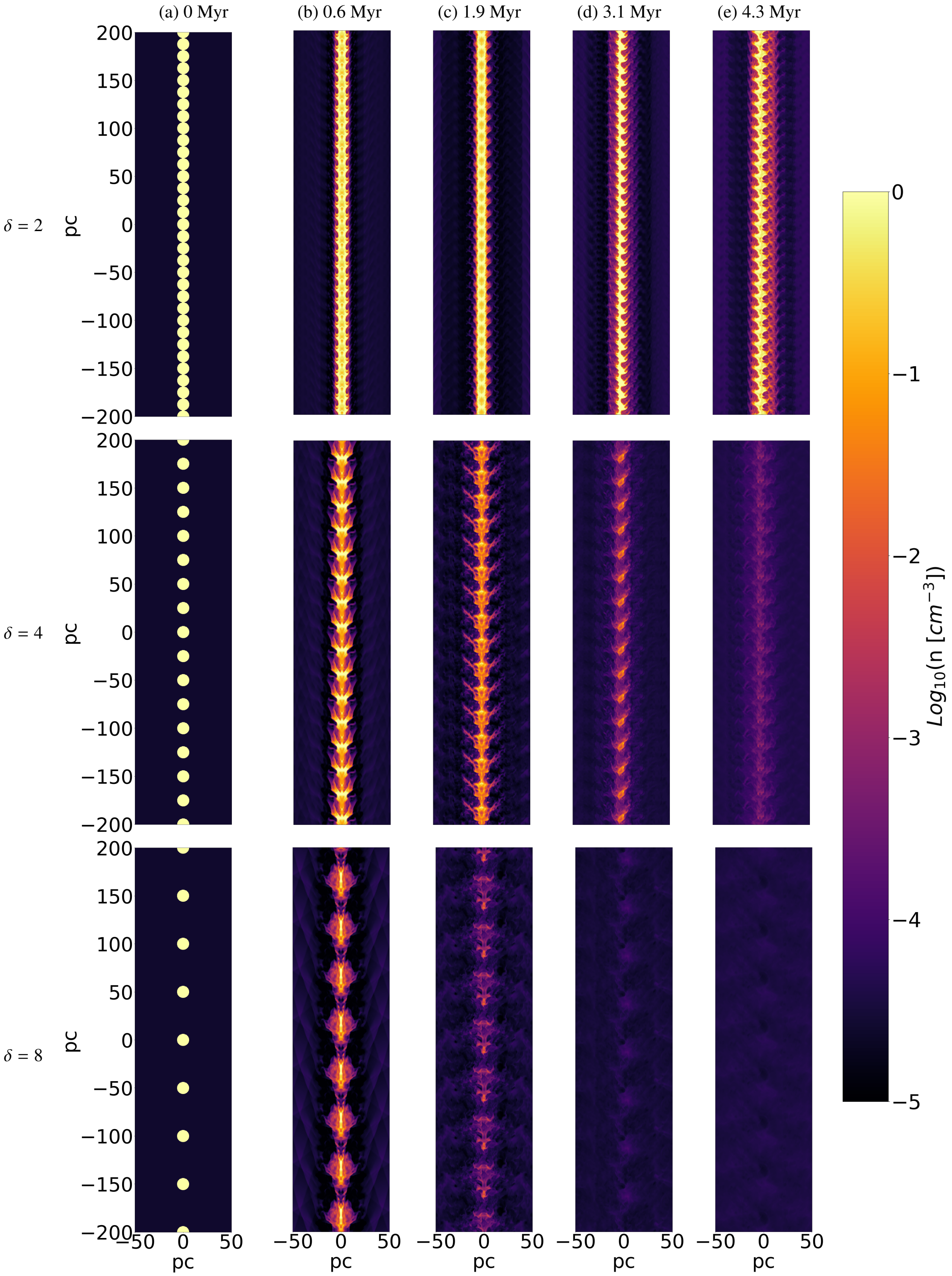

Figure 4.7: Two-dimensional slices of the number density in adiabatic models with different separation values $\delta = 2$ (top panel), $\delta = 4$ (medium panel), and $\delta = 8$ (bottom panel) at five different times through the simulation (columns).

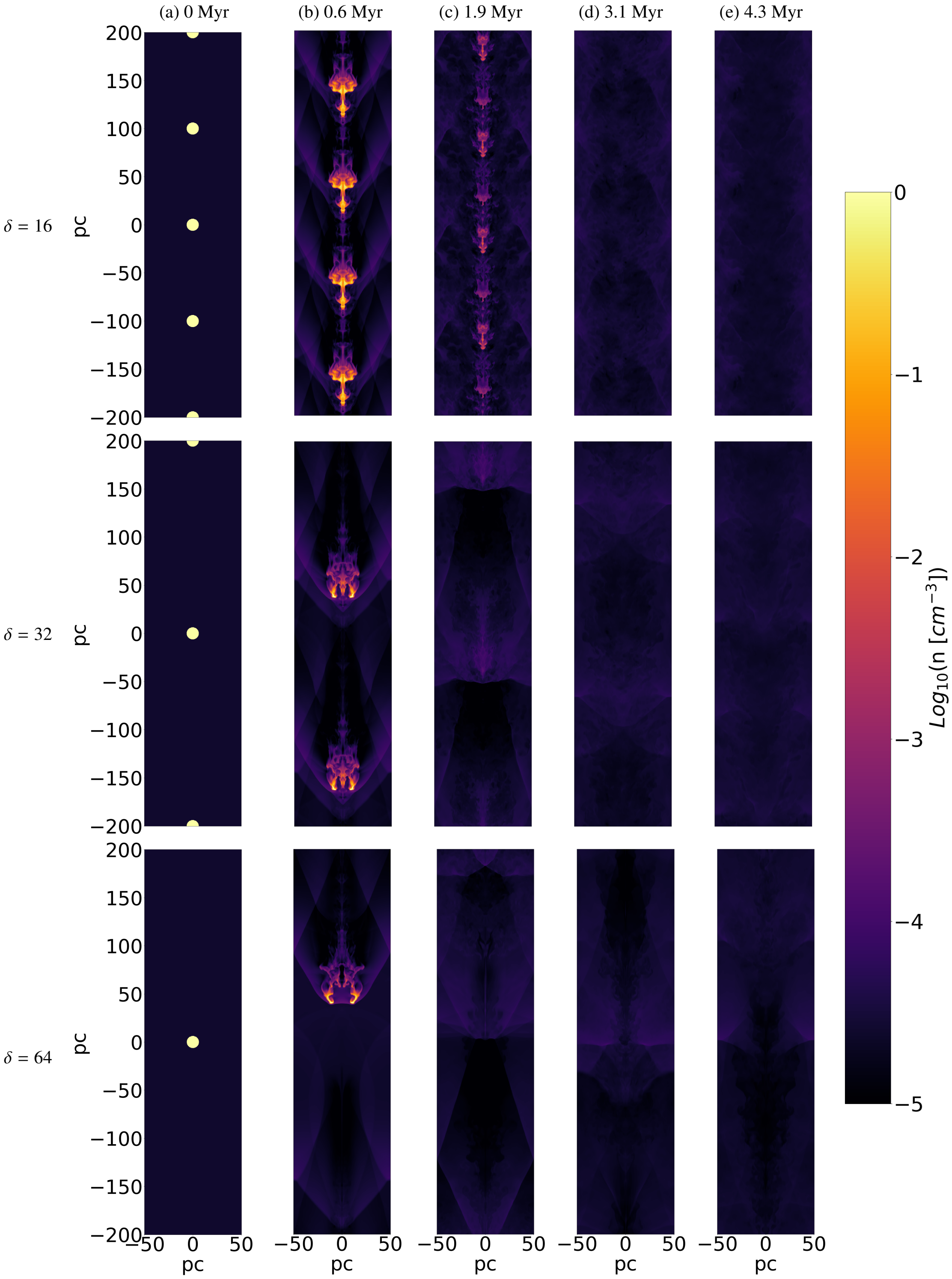

Figure 4.8: Two-dimensional slices of the number density in adiabatic models with different separation values $\delta = 16$ (top panel), $\delta = 32$ (medium panel), and $\delta = 64$ (bottom panel) at five different times through the simulation (columns).

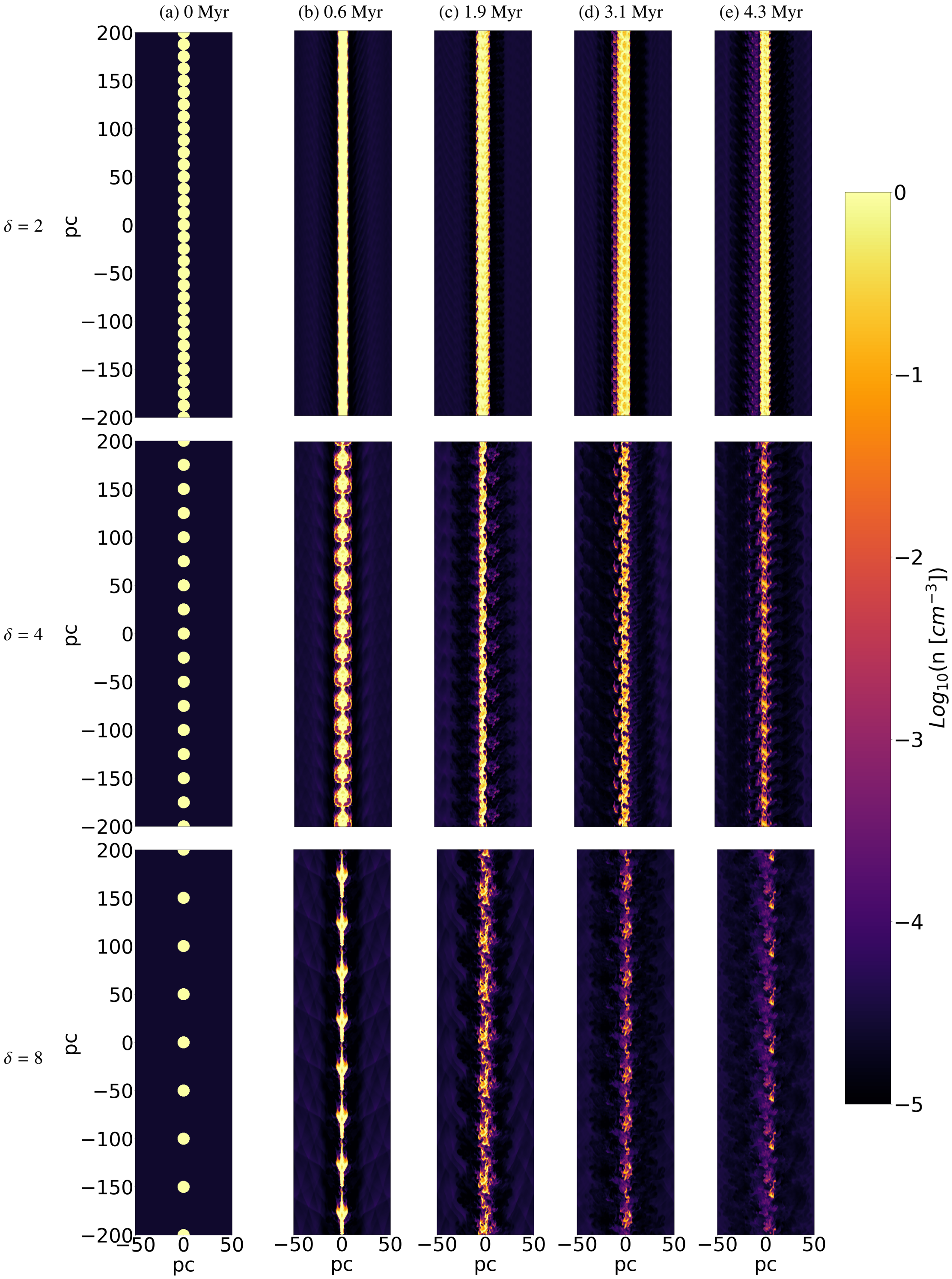

Figure 4.9: Two-dimensional slices of the number density in radiative models with different separation values $\delta = 2$ (top panel), $\delta = 4$ (medium panel), and $\delta = 8$ (bottom panel) at five different times through the simulation (columns).

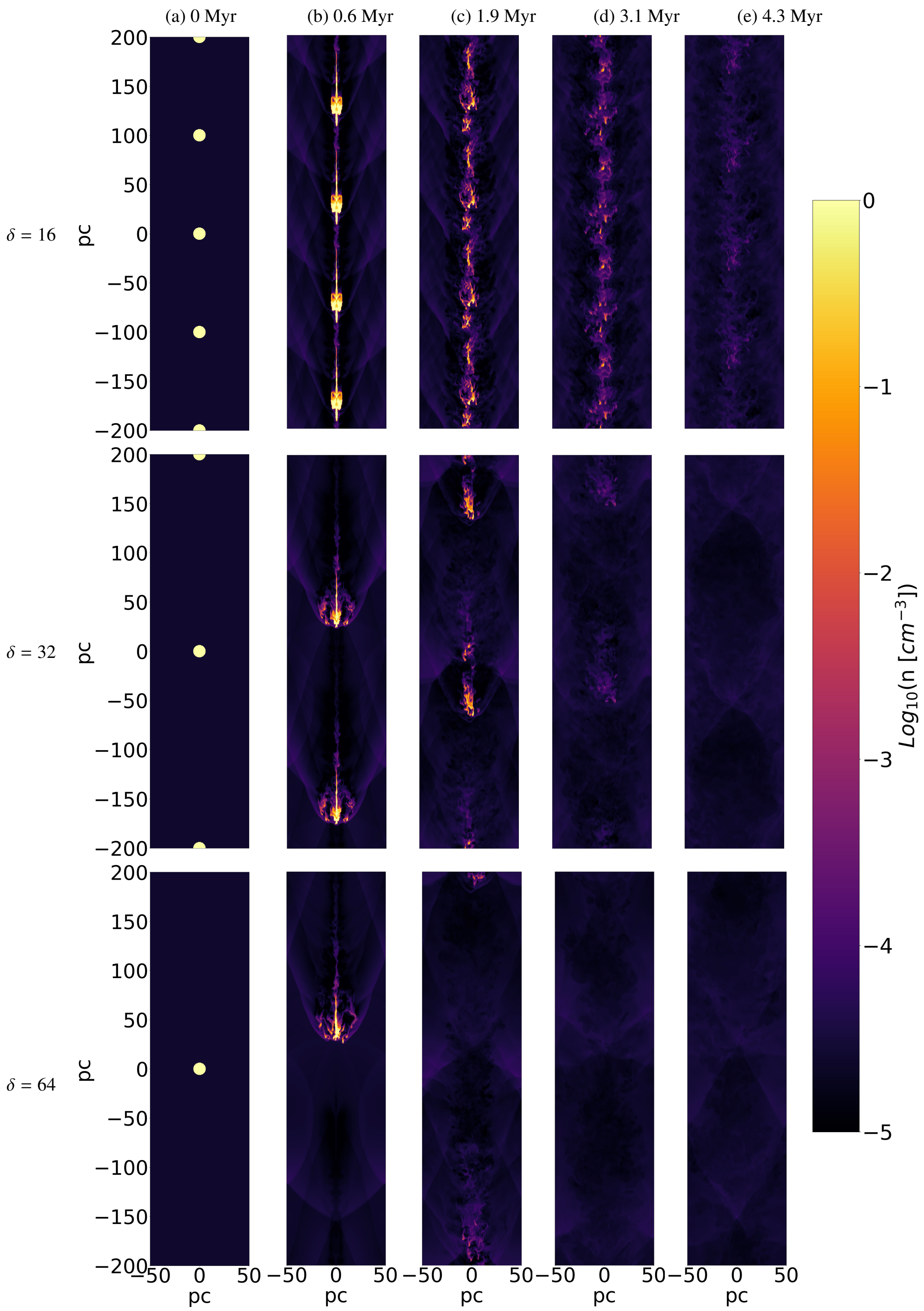

Figure 4.10: Two-dimensional slices of the number density in radiative models with different separation values δ = 16 (top panel), δ = 32 (medium panel), and δ = 64 (bottom panel) at five different times through the simulation (columns).

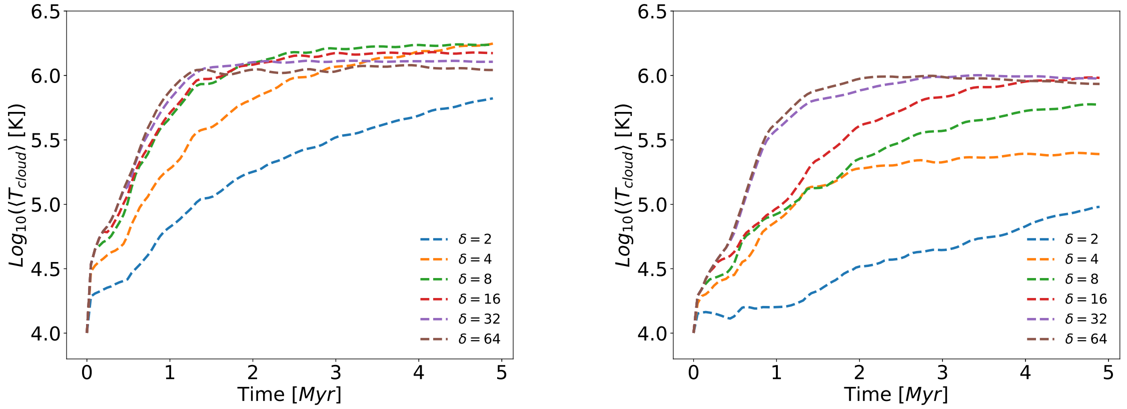

(a) Adiabatic mass-weighted average temperature

(d) Radiative mass-weighted average temperature

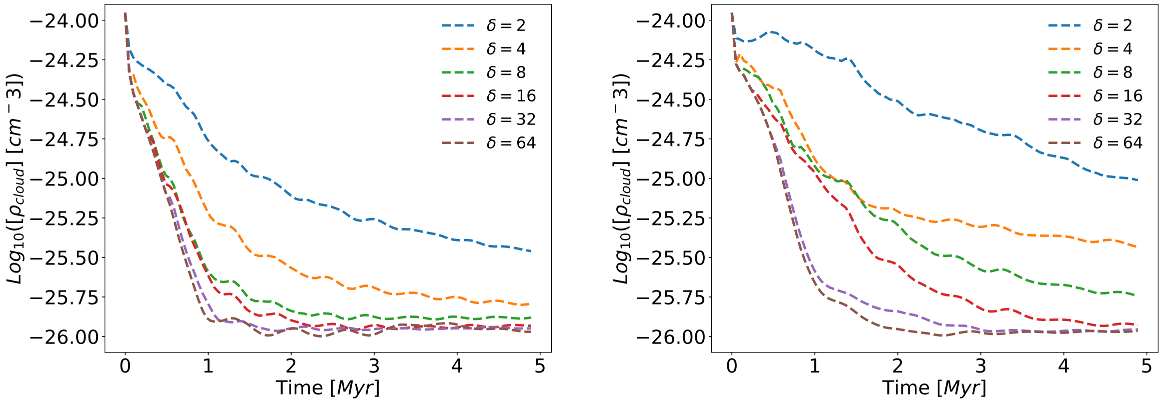

(b) Adiabatic mean density

(e) Radiative mean density

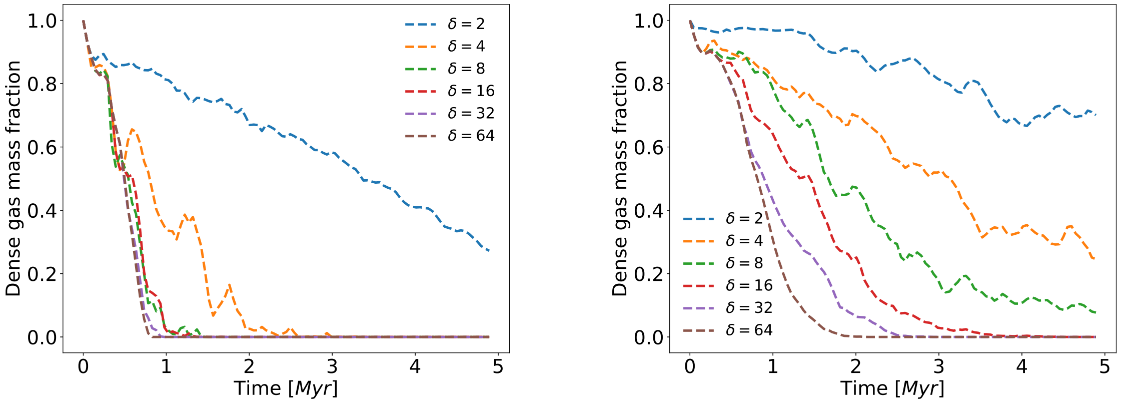

(c) Adiabatic dense gas mass fraction

(f) Radiative dense gas mass fraction

Figure 4.11: Time evolution of the mass-weighted average temperature (top panels), mean density (medium panels), and dense gas mass fraction (bottom panels) for different values of the parameter δ in the adiabatic (left column) and radiative (right column) models.

increasing the inter-cloud separation distance results in a weaker hydrodynamic shielding effect, which leads to the quick destruction of the clouds by drag and instabilities. When the separation value is set to $\delta = 64$, the model can be considered as a model having a quasi-isolated cloud. In such a case, the hydrodynamic shielding effect is practically absent, leading to rapid destruction due to the influence of the background medium. Therefore, there is a significant difference between quasi-isolated clouds that are individually disrupted and those that provide mutual shielding to one another.

In Figure 4.11, we can observe the evolution of various parameters, such as the mass-weighted average temperature, the mean density, and the dense gas mass fraction of cloud material, for both adiabatic and radiative models. It is clear that the hydrodynamic shielding effect plays a crucial role in preserving the dense gas in the stream of cloud material. The trend indicates that the closer the clouds are placed, the best the protection against shredding and erosion of cold material, which in turn avoids a drastic increase in temperature. However, it is important to note that the wind still entrains shear layers, leading to a significant and mild transverse expansion in adiabatic and radiative clouds, respectively. The closely-spaced arrangement has a significant impact on adiabatic clouds, as it offers protection to dense cloud cores by mixed layers of intermediate-density material from the upstream clouds. Therefore, with the separation value $\delta = 2$ the arrangement conserves a dense gas mass of $> 30\%$. Furthermore, this arrangement promotes the precipitation of warm material into the cold phase, contributing to the preservation of gas with temperatures $T < 10^5$ K. This result is in agreement with those represented in Forbes et al. 2019[20], but we have extended the analysis to radiative models.

Compared to adiabatic models, we find that radiative models consistently exhibit a longer lifespan of cloud material. This is due to the effectiveness of radiative cooling and hydrodynamic shielding, which lead to the conservation of $> 70\%$ of the dense gas mass by the end of the simulation period (t$\sim$ 5**Myr**). Additionally, the instabilities are not as effective in the radiative case, as the disruption of dense material and the heating of cold material is reduced, owing to the higher densities, resulting in a low quantity of disturbed material from the clouds. As a result, the dense material is preserved in the stream-like structure, and it not only prevents the growth of new instabilities but also promotes the condensation of cold material.

4.2.3 Cloud Dynamics and Survival

As described in previous sections, the morphology of the clouds is influenced by the variation of the separation distance, δ, and the incorporation of radiative cooling effects. Figure 4.12 showcases the evolution of the mass-weighted velocity, mixing fraction, and cold gas mass fraction of cloud material for both adiabatic and radiative models.

The mixing fraction in both adiabatic and radiative models exhibits significant differences as we change the value of δ. For the radiative model, the cases with larger values $\delta = 16, 32, 64$ are quite similar due to clouds being further apart, resulting in greater disruption by KH and RT instabilities. The adiabatic model has a similar structure, but its mixing is not as efficient as the radiative case. The reason for this is that radiative clouds undergo extremely efficient mixing due to instabilities as well as condensation and cooling-induced pressure gradients. Figure 4.11 illustrates that the thermodynamic paths for these models are similar until t $\sim$ 0.5 Myr, which is when most of the radiative

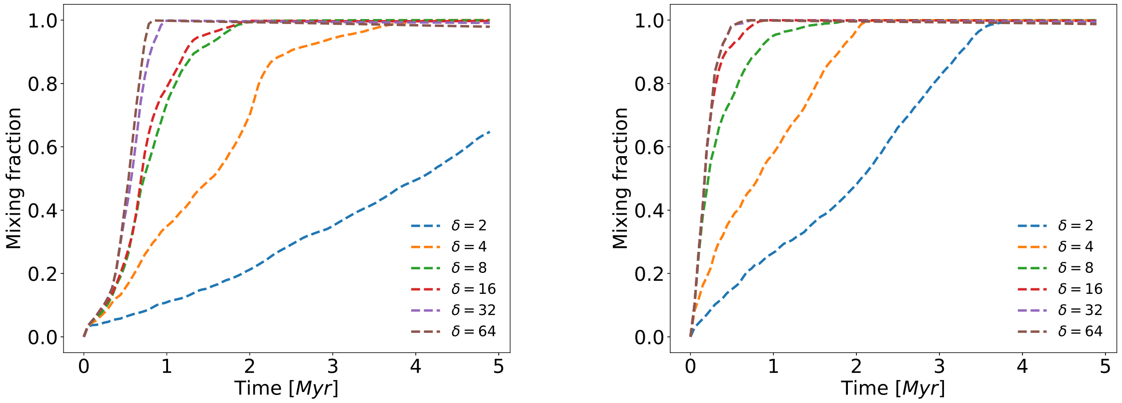

(a) Adiabatic mixing fraction

(d) Radiative mixing fraction

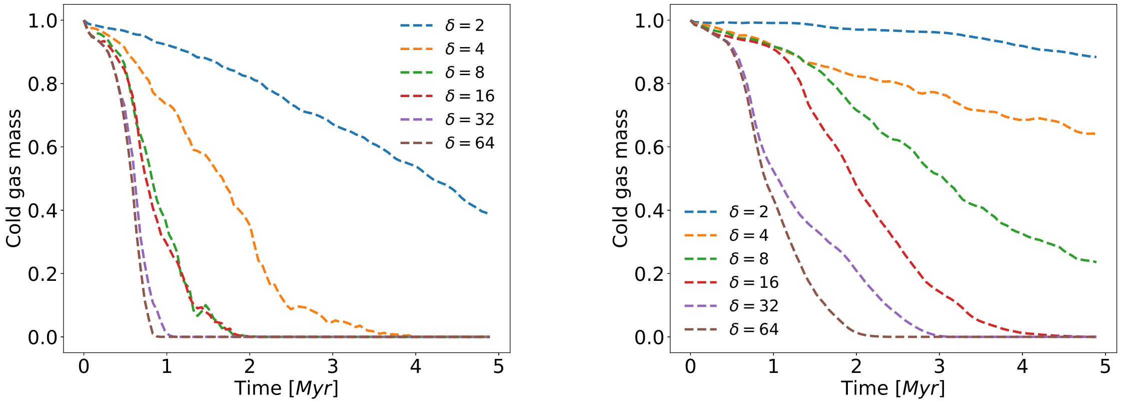

(b) Adiabatic cold gas mass fraction

(e) Radiative cold gas mass fraction

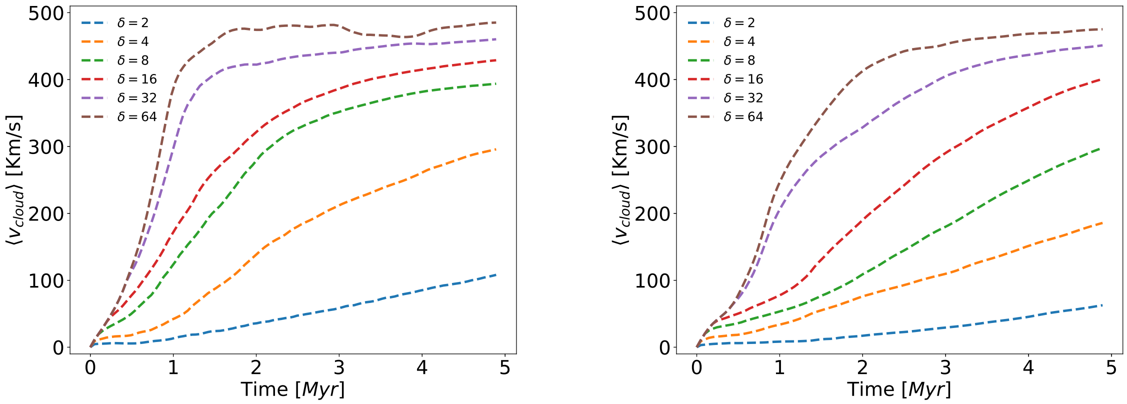

(c) Adiabatic mass-weighted average velocity

(f) Radiative mass-weighted average velocity

Figure 4.12: Time evolution of the mixing fraction (top panels), cold gas mass fraction (medium panels), and mass-weighted average velocity (bottom panels) for different values of the parameter δ in the adiabatic (left column) and radiative (right column) models.

clouds in these models are fully mixed. However, when the clouds are closer together, i.e. $\delta = 2, 4, 8$, the degree of mixing is reduced for both models due to hydrodynamic shielding, which protects the clouds from instabilities. Once again, we can observe that the radiative model is able to mix gas faster, while the adiabatic model cannot mix all of it when clouds are closer to each other. This effect occurs because the radiative model can trigger condensation for all the models, allowing for a high quantity of cold gas mass at the cost of completely mixing all the gas. This is in agreement with the results presented in Banda-Barragán et al. 2021[48].

Adiabatic clouds generally experience a loss of their cold material at $t > 0.9$ Myr, whereas hydrodynamic shielding and cooling mechanisms are effective in the radiative cases, enabling the clouds to survive twice as long as their adiabatic counterparts. For instance, in the cases with small δ values ($\delta = 2$), the adiabatic model retains 40% of its cold gas material at the end of the simulation time (t~ 5 Myr), while the radiative case doubles this amount, retaining over 90% of the cold cloud material. The condensation mechanism proves to be particularly powerful in this regard, helping to maintain cold gas throughout the entire simulation period.

The mass-weighted velocity of the clouds increases as the separation distance δ increases. In other words, clouds that are spaced closer together will take longer to reach a higher velocity. This can be attributed to the fact that a larger δ value results in the formation of larger column densities. As we know from our previous analysis, gas with larger column densities are harder to accelerate via momentum transfer as it has more inertia. We also observe that the adiabatic model has a higher velocity compared to the radiative model. This observation has important implications for the entrainment* of dense gas, which depends on the interplay between radiative processes. Specifically, it suggests that the efficiency of radiative cooling can affect the strength of the hydrodynamic forces acting on the clouds and therefore impact the entrainment of dense gas.

4.2.4 Implications for the Physics of Galactic Winds

In this subsection, we aim to discuss the potential implications of our study for the physics of galactic winds and compare our findings with previous works. Forbes & Lin (2019)[20] conducted a similar set of simulations to ours, focusing mainly on the velocity and the cold gas mass fraction. Their simulations were scale-free and only focused on the hydrodynamics of the gas, which means that the results can be applied if the density contrast and Mach number are similar to what they used. Our simulations, on the other hand, include physical units, time scales, and radiative processes. We also considered a wind with $\mathcal{M}_{wind} = 3.5$, consistent with the CC85 model (see Section 2.1 and Figure 2.1), while Forbes & Lin used both, $\mathcal{M}_{wind} = 0.31$ and $\mathcal{M}_{wind} = 1$, which produced some differences in the behaviour of mass conservation and acceleration. Furthermore, the authors run their simulations for $t_{\rm cross} = 200$, while our work includes simulations for twice that time totalling $t_{\rm cross} = 400$. Despite the different initial conditions, both studies are consistent in showing that adiabatic clouds approach the background wind velocity and have the potential to retain more cold gas mass as the clouds are arranged in closer configurations at t = 0. The implementation of a supersonic hot background in our simulations introduces some differences from the previous work. As observed in the previous study, increasing the $\mathcal{M}$ of the wind reduces the cold gas mass that is retained, while reducing it makes the cloud take more time to accelerate. Additionally, our study reveals that increasing the velocity of the background to supersonic velocities not only decreases the amount the cold gas mass retained by the system but also leads to a longer time for the cloud material to reach the high background velocity. This outcome was expected, particularly in the radiative case, where the increase in the velocity of the clouds highly depends on the formation of density columns.

---

*The process by which material from the ISM becomes mixed and carried by the outflowing galactic wind.

It is necessary to compare our study to other numerical studies that address similar questions in parts of the ISM. For instance, Alūzas et al. (2012)[32] investigated the interaction between a shock and regions containing multiple individual clouds randomly distributed. Their findings indicate that downstream clouds are affected by their interaction with the shock, which results in a lower cloud lifetime compared to clouds located on upstream blocks of the simulation domain. The behaviour of the clouds observed in that study is consistent with the findings presented in our study. While Aluzas randomly distributes groups of clouds in the simulation domain, it is possible that some of that clouds are positioned downstream of each other. As we have demonstrated in this work, that kind of arrangement triggers hydrodynamic shielding, which leads to dense shells of gas due to the protection that upstream clouds provide to downstream clouds.

Another relevant study is the one conducted by Banda-Barragan et al. (2020, 2021)[14 48]. They reported three-dimensional hydrodynamical simulations of a shock interacting with multicloud layers, considering solenoidal and compressive cloud layers, with the inclusion of radiative heating and cooling. Their results show that the dynamics and disruption of a multicloud system depend on the number of cloudlets in the layer. They found that for a more compact system with a high number of cloudlets, turbulence, and mixing are reduced. This is in agreement with our results, as we previously established that if the distance between clouds is decreased, hydrodynamic shielding reduces the effect of dynamical instabilities, which results in a lower mixing fraction. Furthermore, their findings revealed that simulations considering radiative cooling showed that the cooling of mixed gas may explain the presence of dense gas observed in galactic outflows. Our results are consistent with this statement, as we have shown that when we consider radiative processes, dense gas can be maintained for several Myrs by acquiring large column densities. These large column densities are also generated when we have a system with a large number of cloudlets i.e. clouds that are very close to each other. In the compact models presented in that study, the bulk speed is lower than in solenoidal models, as in our simulations where the models with clouds closer to each other diminish the acceleration due to the presence of large column densities. Moreover, the authors of those studies indicated that when we consider radiative cooling, cold material acquires momentum from mixed cloud gas, which is in line with the behaviour of our clouds, where there is not a direct momentum transfer, but momentum is transmitted from the warm phase when this material is condensed to the cold phase.

Let us now direct our attention to research studies that focus on global galaxy simulations. The work carried out by Schneider et al. (2018, 2020)[50 49] presented a set of high-resolution simulations of isolated galaxy models. Their study indicated that mixing and radiative cooling work as sources of fast-moving cool gas, which can be observed in absorption-line studies of outflows around star-forming galaxies. Our work, on the other hand, focuses on patches of the CGM, and it highlights that radiative gas expelled from supernova feedback can be accelerated to velocities of several hundred kilometres per second before being destroyed (due to radiative cooling and hydrodynamic shielding). We previously established that mixing between hot and cold gas provides an effective way of transferring momentum from one phase to another. In agreement with Schneider et al. 2020[49], our models show that gas mixing is deeply connected to dense gas entrainment (i.e. mixing facilitates momentum transfer). This results in a proportional relationship between the mixing fraction and the velocity of the cloud material, thus being consistent with the work of Schneider et al.

An important aspect to highlight is that our work is complementary those previous studies mentioned above, as our models cover a different parameter space, show that hydrodynamic shielding also occurs in radiative scenarios, and provide support to results reported from larger-scale models where the numerical resolution is not sufficient to capture hydrodynamic shielding and separate it from other effects.

4.3 Convergence Analysis and Limitations

4.3.1 Numerical Convergence

In this subsection, we discuss how the numerical resolution of our simulations influences the numerical results that we report in this thesis. We carried out a total of 8 additional simulations for both adiabatic and radiative models. Figure 4.13 and 4.14 show the time evolution of the previous numerical analysis of the adiabatic and radiative model respectively using the standard separation values $\delta = 8, 16$ for the low-(R_8), standard-(R_{16}), and high-(R_{32}) resolution simulations.

The first and third rows show the mass-weighted average temperature, the mean density, and the dense gas mass fraction in cloud material for both models. In the adiabatic model, all the quantities tend to converge, regardless of the separation value being analyzed. However, the thermodynamic path followed by the quantities is not identical, although they do reach similar convergence values across all models. Additionally, the time at which the convergence value is reached is also similar across all the models. In contrast, when radiative processes are considered, there is a spread in the trends observed. For instance, we observe that for $\delta = 16$, both high and standard resolutions show a similar temperature trend, which suggests convergence. However, when it comes to $\delta = 8$, the temperature path varies significantly across all resolutions, and convergence is not achieved. We attribute this to the differences in the mixing profiles in these models, which depend on small-scale phenomena (e.g. turbulence in radiative layers), which do not necessarily converge (see a discussion in Banda-Barragán et al. 2018[2])

The density and the dense gas mass fraction display similar trends, but the lowest resolution model overestimates these quantities for large separation values. Conversely, the standard and high-resolution models exhibit similar behaviour for $\delta = 8$, but they diverge at t $\sim$ 2Myr, causing them to reach different values at later times. Generally, these physical quantities diverge as δ decreases, as cloud-cloud interactions occur more frequently, leading to more condensation and precipitation mechanisms that alter the gas structure. Therefore, for small δ values ($\delta \leq 8$), the numerical quantities are expected to be somewhat divergent. In contrast, for large separation values ($\delta \geq 16$), the standard and high-resolution models exhibit similar behaviour after half the simulation time, leading to convergence for both models. Although differences occur at early times, they are negligible, and we can conclude that convergence is achieved for large δ values.

The second and fourth rows show the mixing fraction, the cold gas mass fraction, and the mass-weighted velocity of cloud material for both models. The mixing fraction in the adiabatic model is influenced by the growth of

(a) Mass-weighted average temperature $\delta = 8$ (e) Mean density $\delta = 8$ (i) Dense gas mass fraction $\delta = 8$

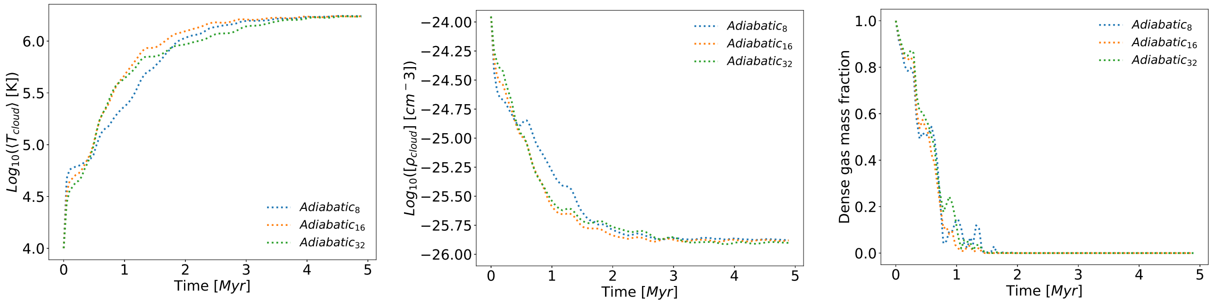

(b) Mixing fraction $\delta = 8$ (f) Cold gas mass fraction $\delta = 8$ (j) Mass-weighted average velocity $\delta = 8$

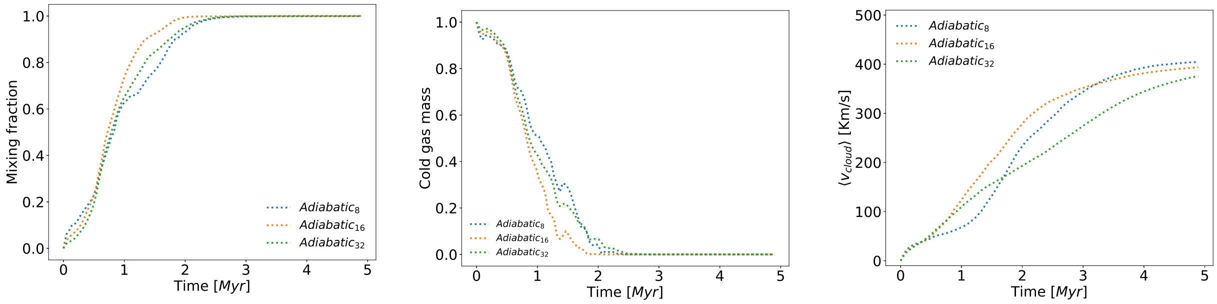

(c) Mass-weighted average temperature $\delta = 16$ (g) Mean density $\delta = 16$ (k) Dense gas mass fraction $\delta = 16$

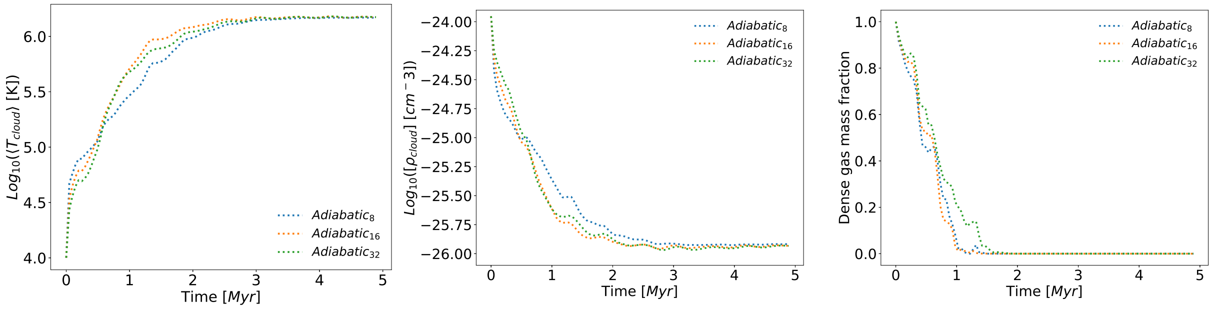

(d) Mixing fraction $\delta = 16$ (h) Cold gas mass fraction $\delta = 16$ (l) Mass-weighted average velocity $\delta = 16$

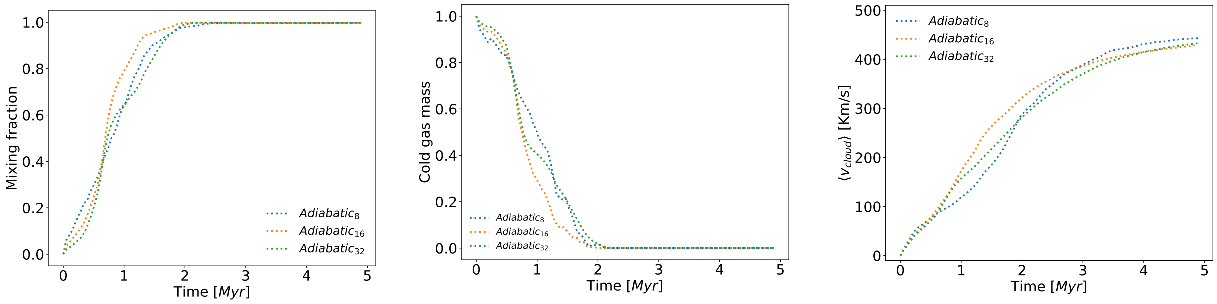

Figure 4.13: Convergence Analysis of the time evolution of the mass-weighted average temperature, mean density, dense gas mass fraction, mixing fraction, cold gas mass fraction, and mass-weighted average velocity of the adiabatic model for $\delta = 8$ (top two rows) and $\delta = 16$ (last two rows).

(a) Mass-weighted average temperature $\delta = 8$ (e) Mean density $\delta = 8$ (i) Dense gas mass fraction $\delta = 8$

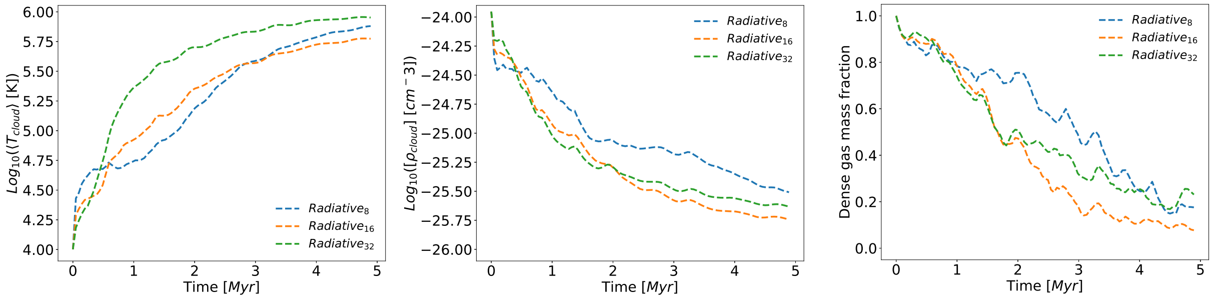

(b) Mixing fraction $\delta = 8$ (f) Cold gas mass fraction $\delta = 8$ (j) Mass-weighted average velocity $\delta = 8$

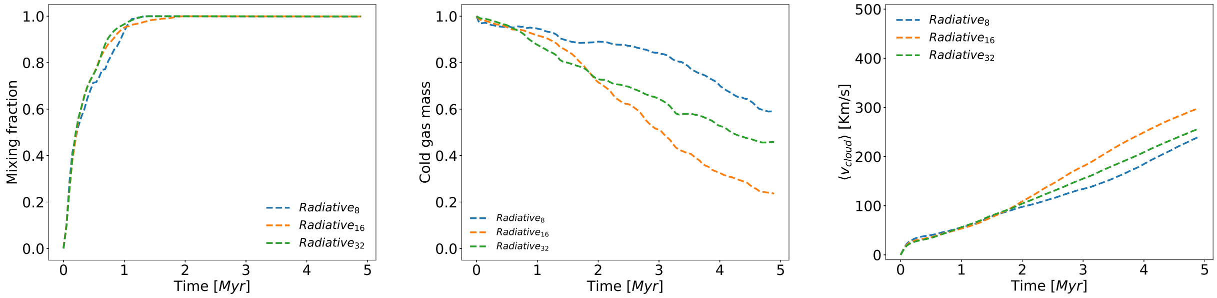

(c) Mass-weighted average temperature $\delta = 16$ (g) Mean density $\delta = 16$ (k) Dense gas mass fraction $\delta = 16$

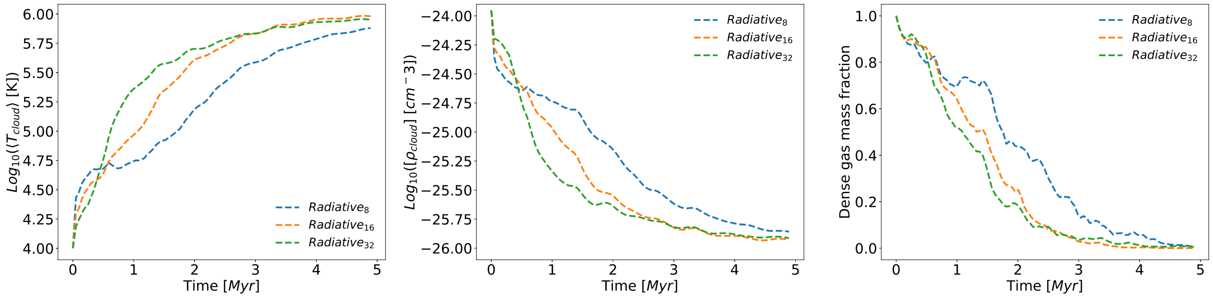

(d) Mixing fraction $\delta = 16$ (h) Cold gas mass fraction $\delta = 16$ (l) Mass-weighted average velocity $\delta = 16$

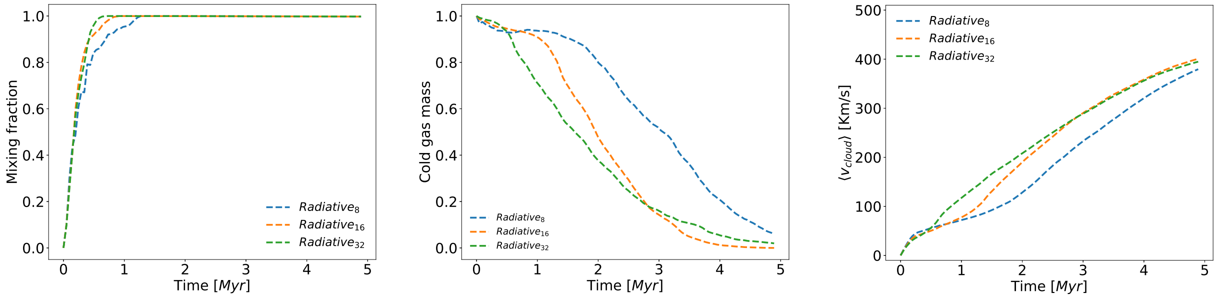

Figure 4.14: Convergence Analysis of the time evolution of the mass-weighted average temperature, mean density, dense gas mass fraction, mixing fraction, cold gas mass fraction, and mass-weighted average velocity of the radiative model for $\delta = 8$ (top two rows) and $\delta = 16$ (last two rows).

dynamical instabilities and turbulence at the gas interfaces, while in the radiative model, it is determined mainly by the cooling efficiency and pressure-gradient forces. Increasing the resolution results in smaller-scale vortical motions, more detailed small-scale eddies, high turbulent mixing, and higher hydrodynamic shielding. Therefore, increasing the resolution is expected to increase mixing in the adiabatic model. However, the curves depicting this parameter exhibit slightly different behavior but overall the process is well captured for all resolutions. In the radiative model, all resolutions can capture the cooling-induced pressure gradients for both large and small δ values. In general, variables that depend on the generation of turbulence (i.e. mixing fraction, cold gas mass fraction, and dense gas mass fraction) exhibit some deviations in the convergence value when resolution is increased for both models, but ultimately, the trends agree and show convergence.

The cold gas mass fraction is closely linked to the average temperature of the cloud material. Hence, it is observed that in the adiabatic model, the cold gas mass fraction converges due to the similarity in the behaviour of temperature, leading to convergence for all the resolutions. However, in the radiative model, there are differences between each resolution as the radiative cooling mechanism plays a crucial role in altering the thermodynamics of the gas. As seen previously for large separation values δ standard and high-resolution simulations converge only with slight deviations. However, for small separation values, there are important deviations in the paths followed by each simulation. Since the temperature does not converge, the cold gas mass fraction exhibits similar behaviour with all the simulations having different paths and values at the end of the simulation time. In general, for thermodynamic quantities and small δ values, numerical quantities tend to be more divergent as they depend on smaller-scale effects.

In the adiabatic models, the mass-weighted average velocity of cloud material exhibits convergence. The standard resolution is sufficient to capture the dynamics of the gas and how it is accelerated by the supersonic hot background. Similarly, in the radiative models, the behaviour of the cloud velocity remains consistent regardless of the chosen resolution. As previously discussed, the acceleration of radiative clouds is not due to direct momentum transfer but rather momentum conservation from warm material. Based on the evolution of these specific variables, we can conclude that all resolutions correctly capture the dynamics of the multi-cloud system for the adiabatic and radiative systems.

4.3.2 Limitations of our Study

While the analysis of hydrodynamic interactions between two gas phases (cold clouds and hot winds) provides an overall view of the galactic outflows, it is essential to acknowledge the limitations of our numerical work due to the exclusion of additional physics in our study.

Self-gravity is one such aspects, not included in our models, that may affect the evolution of clouds. Our radiative clouds undergo compression, so some regions of them could become marginally gravitationally unstable had self-gravity been included. This phenomenon has been observed in our specific context of cold, dense spherical clouds moving through a hot medium (see Murray et al. 1993[51]). Despite this, KH instabilities and the generation of turbulence may prevent the gravitational collapse of such regions, so we think the role of self-gravity for the cloud parameters included in our models would still be secondary compared to hydrodynamic shielding and shredding. For other initial conditions with denser clouds this may not be the case, so future work would be needed to evaluate such regime.

In other scenarios, it has been proved that the inclusion of electron thermal conduction has a significant impact on the way clouds interact with the wind, leading to changes in their morphology, mass loss rate, and velocity (see Brüggen & Scannapieco 2016[52]). The acceleration of cold clouds by the ambient background is hindered by thermal conduction, which can alter the dynamics of the system in various ways. Electron thermal conduction could also influence hydrodynamic shielding as it can lead to the evaporation of the outer layers of the clouds, but its role can be complex and hard to predict, so future numerical work on wind-multicloud models with conduction is warranted.

In addition, it is important to note that this study did not incorporate magnetic fields. Magnetohydrodynamic (MHD) scenarios are known to significantly affect the dynamics and survival of dense gas (see Banda-Barragan et al. 2018[2]). The initial topology of the magnetic field can lead to different morphologies and turbulent properties in the cloud material. For instance, models with magnetic field components aligned with flow direction exhibit a higher mixing fraction and velocity dispersion than models with magnetic field components transverse to the flow. On the other hand, magnetic fields oblique to the flow direction result in a more elongated, less turbulent gas tail. Therefore, it is crucial that future studies conduct MHD simulations of wind-multicloud systems that incorporate these additional physics to further investigate the magnetic field effects on cloud dynamics and hydrodynamic shielding.

Chapter 5

Conclusions & Outlook

Galaxy formation and evolution involve several complex mechanisms. One of such mechanisms is the ejection of stellar-driven galactic winds, which are responsible for regulating the mass and metal content of galaxies. Small-scale wind-cloud models have been significant in comprehending the empirical relationship between clouds and the surrounding hot wind gas. However, the ease with which cold clouds can be disrupted in simulations represents a significant challenge in explaining the observations of cold gas in galactic winds. Recent surveys of quasar absorption lines have identified a considerable amount of gas with low ionization states at significant distances from the centres of galaxies, which is puzzling given how efficiently cold clouds can be disrupted. The aim of this study was then to evaluate the efficiency of hydrodynamic shielding in preserving dense cold gas by means of numerical models of systems of multiple clouds with $T\sim 10^4$K embedded in a hot supersonic ambient wind with $T\sim 10^6$K and $\mathcal{M} = 3.5$. This research was carried out by analyzing the behaviour of multicloud systems with different separation distances (δ) between the clouds. The main findings of this thesis are summarised below:

- The overall evolution of wind-multicloud models can be divided into four distinct stages: 1) The wind material collides with the front surface of the upstream clouds, producing both reflected and refracted shocks; 2) Clouds begin to lose mass through stripping caused by KH instabilities from their surface layers; 3) The upstream motion of the wind leads to the collision between the filamentary tails of upstream clouds with the cores of downstream clouds; 4) Clouds have undergone a substantial mass loss, and their acceleration has reached a level that triggers the growth of RT instabilities. These instabilities ultimately cause the destruction of clouds, as low-density bubbles penetrate dense layers of remaining cloud material (see Section 4.1.1).
- Our models of adiabatic clouds, which lack an efficient energy release mechanism, are eventually heated and shredded. In contrast, or models with radiative clouds show that efficient cooling can remove energy that would otherwise be converted into heat. This, combined with cooling-induced pressure gradients, promotes condensation and mixing, which aid the survival and re-formation of dense clouds as the cold gas is shielded from instabilities. As a result, the lifetime of dense and cold material in radiative clouds is in all cases longer than that of their adiabatic counterparts (see Section 4.1.2 and 4.1.3).

- Adiabatic clouds are rapidly destroyed due to the presence of KH instabilities, which make it impossible for them to retain cold gas. Conversely, radiative clouds exhibit a multiphase structure characterized by both a cooler, denser gas phase, and a lower-density, higher-temperature gas phase. The denser material of radiative clouds is protected from instabilities thanks to the higher column densities of cold gas. The evolution of the mixing fraction is also different between adiabatic and radiative models. In adiabatic models, mixing occurs due to KH and RT instabilities, while radiative clouds experience additional mixing due to cooling-induced pressure gradients. The condensation process occurs when warm gas precipitates into a colder and denser material as a result of efficient cooling (see Section 4.1.4).

- The velocities of adiabatic clouds are higher than those of radiative clouds, as gas with higher column densities is more difficult to accelerate via momentum transfer. Adiabatic clouds obtain their acceleration through direct momentum transfer, whereas radiative clouds retain some of the momentum present in the warm phase as they condense back into the cold phase thanks to efficient cooling (see Section 4.1.4).

- Dynamic and thermodynamic differences arise when we change the initial separation distance between the clouds, δ. The morphology of downstream clouds is not only influenced by the wind but also by the tails of upstream clouds that eventually collide with them. The interaction between the hot wind, clouds, and gas that has already interacted with the upstream cloud's material further affects the evolution. When the separation value is decreased, our models show that there is a significant increase in hydrodynamic shielding, as the effective drag force acting on individual downstream clouds is reduced. This leads to the preservation of dense material for a longer period of time. Closely-spaced arrangements have a substantial impact on the clouds, as they offer protection to the dense cloud cores from the mixed turbulent layers of intermediate-density material produced by upstream clouds. This material is preserved in stream-like structures, reducing the growth rate of instabilities while also facilitating the condensation of cold material (see Section 4.2.1 and 4.2.2).

- The degree of mixing between clouds is linked to their separation distance. The further apart the clouds are, the greater the chance of generating dynamic instabilities, which enhances the degree of mixing. When clouds are closer to each other, the condensation mechanism is particularly powerful as the effective drag forces are drastically reduced, helping to maintain the cold gas throughout the entire simulation period. The mass-weighted velocity of cloud material decreases as the separation value δ decreases, as tighter arrangements trigger the generation of large column densities. This occurs as gas with larger column densities is more difficult to accelerate via momentum transfer (see Section 4.2.3).

- When examining adiabatic models, we found that regardless of the separation distance being considered, there is overall convergence in all the quantities. When radiative processes are taken into account, the standard-resolution and high-resolution models display a similar behaviour for large separation values, particularly after half the simulation time, leading to convergence. However, when it comes to small separation values, variables that depend on turbulence generation initially exhibit slight deviations between standard and high resolution, but as we move forward in time, they ultimately converge. The physical quantities that are affected by condensation and precipitation mechanism exhibit divergence as δ decreases, as cloud-cloud interaction occurs more frequently (see Section 4.3).

Overall, our study demonstrates that incorporating radiative cooling in wind-multicloud simulations explains the multiphase nature of galactic winds and enhances the effectiveness of hydrodynamic shielding. A multiphase gas forms, where regions of cold, dense gas coexist with warm and hot, low-density gas. In addition, shielding increases the lifetime of cold clouds and preserves dense material, albeit at the cost of reducing its velocity. Future research should consider incorporating additional physical processes to further enhance our understanding of multicloud system dynamics and hydrodynamic shielding. The inclusion of magnetic fields, self-gravity, and electron thermal conduction can provide valuable insights into how these factors influence dense gas survival.

Bibliography

[1] Tumlinson, J.; Peeples, M. S.; Werk, J. K. The Circumgalactic Medium. **2017**, *55*, 389–432.

[2] Banda-Barragán, W. E.; Federrath, C.; Crocker, R. M.; Bicknell, G. V. Filament formation in wind-cloud interactions- II. Clouds with turbulent density, velocity, and magnetic fields. **2018**, *473*, 3454–3489.

[3] Shopbell, P. L.; Bland-Hawthorn, J. The Asymmetric Wind in M82. *The Astrophysical Journal* **1998**, *493*, 129.

[4] Scannapieco, E.; Thacker, R. J.; Davis, M. High-Redshift Galaxy Outflows and the Formation of Dwarf Galaxies. **2001**, *557*, 605–615.

[5] Kaviraj, S.; Laigle, C.; Kimm, T.; Devriendt, J. E. G.; Dubois, Y.; Pichon, C.; Slyz, A.; Chisari, E.; Peirani, S. The Horizon-AGN simulation: evolution of galaxy properties over cosmic time. *Monthly Notices of the Royal Astronomical Society* **2017**, *467*, 4739–4752.

[6] Tripp, T. M.; Meiring, J. D.; Prochaska, J. X.; Willmer, C. N. A.; Howk, J. C.; Werk, J. K.; Jenkins, E. B.; Bowen, D. V.; Lehner, N.; Sembach, K. R.; Thom, C.; Tumlinson, J. The Hidden Mass and Large Spatial Extent of a Post-Starburst Galaxy Outflow. *Science* **2011**, *334*, 952–955.

[7] Teodoro, E. M. D.; McClure-Griffiths, N. M.; Lockman, F. J.; Denbo, S. R.; Endsley, R.; Ford, H. A.; Harrington, K. Blowing in the Milky Way Wind: Neutral Hydrogen Clouds Tracing the Galactic Nuclear Outflow. *The Astrophysical Journal* **2018**, *855*, 33.

[8] Salak, D.; Tomiyasu, Y.; Nakai, N.; Kuno, N.; Miyamoto, Y.; Kaneko, H. Dense Molecular Gas in the Starburst Nucleus of NGC 1808. *The Astrophysical Journal* **2018**, *856*, 97.

[9] Ballone, A.; Schartmann, M.; Burkert, A.; Gillessen, S.; Genzel, R.; Fritz, T. K.; Eisenhauer, F.; Pfuhl, O.; Ott, T. Hydrodynamical Simulations of a Compact Source Scenario for the Galactic Center Cloud G2. **2013**, *776*, 13.

[10] Mendis, D. A.; Horányi, M. The Global Morphology of the Solar Wind Interaction with Comet Churyumov-Gerasimenko. **2014**, *794*, 14.

[11] Klein, R. I.; McKee, C. F.; Colella, P. On the Hydrodynamic Interaction of Shock Waves with Interstellar Clouds. I. Nonradiative Shocks in Small Clouds. **1994**, *420*, 213.

[12] Cottle, J.; Scannapieco, E.; Brüggen, M.; Banda-Barragán, W.; Federrath, C. The Launching of Cold Clouds by Galaxy Outflows. III. The Influence of Magnetic Fields. **2020**, *892*, 59.

[13] Gregori, G.; Miniati, F.; Ryu, D.; Jones, T. W. Three-dimensional Magnetohydrodynamic Numerical Simulations of Cloud-Wind Interactions. *The Astrophysical Journal* **2000**, *543*, 775.

[14] Banda-Barragán, W. E.; Brüggen, M.; Federrath, C.; Wagner, A. Y.; Scannapieco, E.; Cottle, J. Shock–multicloud interactions in galactic outflows – I. Cloud layers with lognormal density distributions. *Monthly Notices of the Royal Astronomical Society* **2020**, *499*, 2173–2195.

[15] Schneider, E. E.; Robertson, B. E. Hydrodynamical Coupling of Mass and Momentum in Multiphase Galactic Winds. **2017**, *834*, 144.

[16] Cooper, J. L.; Bicknell, G. V.; Sutherland, R. S.; Bland-Hawthorn, J. Starburst-Driven Galactic Winds: Filament Formation and Emission Processes. **2009**, *703*, 330–347.

[17] Nakamura, F.; McKee, C. F.; Klein, R. I.; Fisher, R. T. On the Hydrodynamic Interaction of Shock Waves with Interstellar Clouds. II. The Effect of Smooth Cloud Boundaries on Cloud Destruction and Cloud Turbulence. *The Astrophysical Journal Supplement Series* **2006**, *164*, 477.

[18] Banda-Barragán, W. E.; Parkin, E. R.; Federrath, C.; Crocker, R. M.; Bicknell, G. V. Filament formation in wind–cloud interactions – I. Spherical clouds in uniform magnetic fields. *Monthly Notices of the Royal Astronomical Society* **2015**, *455*, 1309–1333.

[19] Sparre, M.; Pfrommer, C.; Vogelsberger, M. The physics of multiphase gas flows: fragmentation of a radiatively cooling gas cloud in a hot wind. *Monthly Notices of the Royal Astronomical Society* **2018**, *482*, 5401–5421.

[20] Forbes, J. C.; Lin, D. N. C. Hydrodynamic Shielding and the Survival of Cold Streams. *The Astronomical Journal* **2019**, *158*, 124.

[21] Tumlinson, J.; Thom, C.; Werk, J. K.; Prochaska, J. X.; Tripp, T. M.; Weinberg, D. H.; Peeples, M. S.; O'Meara, J. M.; Oppenheimer, B. D.; Meiring, J. D.; Katz, N. S.; Davé, R.; Ford, A. B.; Sembach, K. R. The Large, Oxygen-Rich Halos of Star-Forming Galaxies Are a Major Reservoir of Galactic Metals. *Science* **2011**, *334*, 948–952.

[22] Pfuhl, O.; Gillessen, S.; Eisenhauer, F.; Genzel, R.; Plewa, P. M.; Ott, T.; Ballone, A.; Schartmann, M.; Burkert, A.; Fritz, T. K.; Sari, R.; Steinberg, E.; Madigan, A.-M. The Galactic Center Cloud G2 and its Gas Streamer. **2015**, *798*, 111.

[23] Casavecchia, B.; Banda-Barragán, W. E.; Brüggen, M.; Brighenti, F. Absorption spectra from galactic wind models: a framework to link PLUTO simulations to TRIDENT. *IAU Symposium* **2023**, *362*, 56–63.

[24] Heckman, T. M.; Thompson, T. A. Galactic Winds and the Role Played by Massive Stars. *arXiv e-prints* **2017**, arXiv:1701.09062.

[25] Krumholz, M. R.; Burkhart, B.; Forbes, J. C.; Crocker, R. M. A unified model for galactic discs: star formation, turbulence driving, and mass transport. **2018**, *477*, 2716–2740.

[26] Laganá, T. F.; Dupke, R. A.; Sodré, J., L.; Lima Neto, G. B.; Durret, F. The optical/X-ray connection: intra-cluster medium iron content and galaxy optical luminosity in 20 galaxy clusters. **2009**, *394*, 357–366.

[27] McKee, C. F.; Ostriker, J. P. A theory of the interstellar medium: three components regulated by supernova explosions in an inhomogeneous substrate. **1977**, *218*, 148–169.

[28] Chevalier, R. A.; Clegg, A. W. Wind from a starburst galaxy nucleus. **1985**, *317*, 44–45.

[29] Zhang, D. A Review of the Theory of Galactic Winds Driven by Stellar Feedback. *Galaxies* **2018**, *6*.

[30] Strickland, D. K.; Heckman, T. M. Supernova Feedback Efficiency and Mass Loading in the Starburst and Galactic Superwind Exemplar M82. **2009**, *697*, 2030–2056.

[31] Bustard, C.; Zweibel, E. G.; D'Onghia, E. A VERSATILE FAMILY OF GALACTIC WIND MODELS. *The Astrophysical Journal* **2016**, *819*, 29.

[32] Alūzas, R.; Pittard, J. M.; Hartquist, T. W.; Falle, S. A. E. G.; Langton, R. Numerical simulations of shocks encountering clumpy regions. **2012**, *425*, 2212–2227.

[33] Alūzas, R.; Pittard, J. M.; Falle, S. A. E. G.; Hartquist, T. W. Numerical simulations of a shock interacting with multiple magnetized clouds. **2014**, *444*, 971–993.

[34] Armillotta, L.; Fraternali, F.; Werk, J. K.; Prochaska, J. X.; Marinacci, F. The survival of gas clouds in the circumgalactic medium of Milky Way-like galaxies. **2017**, *470*, 114–125.

[35] de la Cruz, L. M.; Schneider, E. E.; Ostriker, E. C. Synthetic Absorption Lines from Simulations of Multiphase Gas in Galactic Winds. **2021**, *919*, 112.

[36] F.R.S., S. W. T. XLVI. Hydrokinetic solutions and observations. *The London, Edinburgh, and Dublin Philosophical Magazine and Journal of Science* **1871**, *42*, 362–377.

[37] Helmholtz, P. XLIII. On discontinuous movements of fluids. *The London, Edinburgh, and Dublin Philosophical Magazine and Journal of Science* **1868**, *36*, 337–346.

[38] Chandrasekhar, S. *Hydrodynamic and Hydromagnetic Stability, By S. Chandrasekhar*; International series of monographs on physics; 1961.

[39] Rayleigh, Investigation of the Character of the Equilibrium of an Incompressible Heavy Fluid of Variable Density. *Proceedings of the London Mathematical Society* **1882**, *s1-14*, 170–177.

[40] Taylor, G. I. The instability of liquid surfaces when accelerated in a direction perpendicular to their planes. I. *Proceedings of the Royal Society of London. Series A. Mathematical and Physical Sciences* **1950**, *201*, 192–196.

[41] Draine, B. T. *Physics of the Interstellar and Intergalactic Medium*; 2011.

[42] Wiersma, R. P. C.; Schaye, J.; Smith, B. D. The effect of photoionization on the cooling rates of enriched, astrophysical plasmas. *Monthly Notices of the Royal Astronomical Society* **2009**, *393*, 99–107.

[43] Smith, B. D.; Bryan, G. L.; Glover, S. C. O.; Goldbaum, N. J.; Turk, M. J.; Regan, J.; Wise, J. H.; Schive, H.-Y.; Abel, T.; Emerick, A.; O'Shea, B. W.; Anninos, P.; Hummels, C. B.; Khochfar, S. GRACKLE: a chemistry and cooling library for astrophysics. **2017**, *466*, 2217–2234.

[44] Mignone, A.; Bodo, G.; Massaglia, S.; Matsakos, T.; Tesileanu, O.; Zanni, C.; Ferrari, A. PLUTO: A Numerical Code for Computational Astrophysics. *The Astrophysical Journal Supplement Series* **2007**, *170*, 228–242.

[45] Toro, E. F.; Spruce, M.; Speares, W. Restoration of the contact surface in the HLL-Riemann solver. *Shock waves* **1994**, *4*, 25–34.

[46] Mignone, A. High-order conservative reconstruction schemes for finite volume methods in cylindrical and spherical coordinates. *Journal of Computational Physics* **2014**, *270*, 784–814.

[47] Heyer, M. *et al.* The Dense Gas Mass Fraction and the Relationship to Star Formation in M51. *The Astrophysical Journal* **2022**, *930*, 170.

[48] Banda-Barragán, W. E.; Brüggen, M.; Heesen, V.; Scannapieco, E.; Cottle, J.; Federrath, C.; Wagner, A. Y. Shock–multicloud interactions in galactic outflows – II. Radiative fractal clouds and cold gas thermodynamics. *Monthly Notices of the Royal Astronomical Society* **2021**, *506*, 5658–5680.

[49] Schneider, E. E.; Ostriker, E. C.; Robertson, B. E.; Thompson, T. A. The Physical Nature of Starburst-driven Galactic Outflows. **2020**, *895*, 43.

[50] Schneider, E. E.; Robertson, B. E.; Thompson, T. A. Production of Cool Gas in Thermally Driven Outflows. **2018**, *862*, 56.

[51] Murray, S. D.; White, S. D. M.; Blondin, J. M.; Lin, D. N. C. Dynamical Instabilities in Two-Phase Media and the Minimum Masses of Stellar Systems. **1993**, *407*, 588.

[52] Brüggen, M.; Scannapieco, E. The Launching of Cold Clouds by Galaxy Outflows. II. The Role of Thermal Conduction. **2016**, *822*, 31.